Origin and Propagation of a Disturbance Associated with an African Easterly Wave as a Precursor of Hurricane Alberto (2000)

YUH-LANG LIN, KATIE E. ROBERTSON, AND CHRISTOPHER M. HILL

Department of Marine, Earth, and Atmospheric Sciences, North Carolina State University, Raleigh, North Carolina

(Manuscript received 18 February 2005, in final form 30 April 2005)

ABSTRACT

In this study, it is proposed that mesoscale convective complexes (MCCs) and a mesovortex (MV) were embedded within a wavelike disturbance over North Africa that led to the genesis of Hurricane Alberto (2000). The wavelike disturbance observed may be classified as an African easterly wave (AEW). Based on the cloud-top area and brightness values observed from infrared satellite data, four genesis and three lysis stages are identified within a cycle of moist convection associated with the pre-Alberto disturbance. The availability of water vapor is the most essential factor controlling the convective cycle of the pre-Alberto disturbance over the African continent. The presence of significant topography also contributes to the generation or decay of the associated MCCs through regulation of the water vapor supply. Further analysis of Meteosat satellite imagery reveals that the incipient disturbances for 23 of 34 eastern Atlantic tropical cyclones originated from the Ethiopian highlands (EH) region during the period of 1990–2001.

The pre-Alberto disturbance was found to have exhibited characteristics of an AEW. At the EH, there existed two modes of disturbance development: a stationary mode and a propagating mode. The stationary mode corresponded with the generation of moist convection over the EH triggered by diurnally variant sensible heating, while the propagating mode corresponded with the generation and propagation of MVs and mesoscale convective systems (MCSs) from the lee side of the EH over a period of about 2 to 3 days. These components of the disturbance propagated westward together within an AEW train at an average speed of 11.6 m s^{-1}. The average wavelength was roughly estimated to be about 2200 km.

To prove that disturbances generated at the EH are indeed AEWs, the NCAR Regional Climate Model Version 3.0 is adopted to simulate the event. The simulated fields showed that both the propagating wave and stationary mountain wave modes were present, the convection was generated over the EH, and the pre-Alberto disturbance was generated near the lee of the EH. In addition, the convective cycle detected from NCEP reanalysis data was also reflected in the simulated fields. The simulated AEW possesses similar wave characteristics as the observed pre-Alberto disturbance.

1. Introduction

A significant number of tropical cyclones that have occurred over the eastern Atlantic Ocean, particularly near the Cape Verde Islands, can be traced back to the African continent as mesoscale convective complexes (MCCs) (e.g., Laing and Fritsch 1993; Simpson et al. 1997; Gray 1998). Early studies had established African easterly waves (AEWs) as the source disturbances for the development of Atlantic tropical cyclones (e.g., Piersig 1936; Regula 1936; Riehl 1945; Gray 1968). Through the analysis of more detailed satellite and observational data, Simpson et al. (1968) and Carlson (1969) traced the genesis of some Atlantic tropical cyclones from disturbances first observed over western and central Africa around 10°N. As Laing and Fritsch (1993) pointed out, understanding the origin of these disturbances has important implications for understanding the dynamics of tropical cyclogenesis over the tropical eastern Atlantic Ocean.

AEWs possess characteristics similar to those of the easterly waves found over the Pacific Ocean (e.g., Riehl 1948; Yanai et al. 1968; Wallace and Chang 1969; Nitta 1970; Chang et al. 1970). Riehl (1948) found the presence of westward propagating wave disturbances over the equatorial Pacific Ocean to precede the genesis of typhoons. In the same light, Chang (1970) constructed a

Corresponding author address: Dr. Yuh-Lang Lin, Dept. MEAS, NCSU, 1125 Jordan Hall, Faucette Drive, Raleigh, NC 27695-8208.
E-mail: yl_lin@ncsu.edu

© 2005 American Meteorological Society

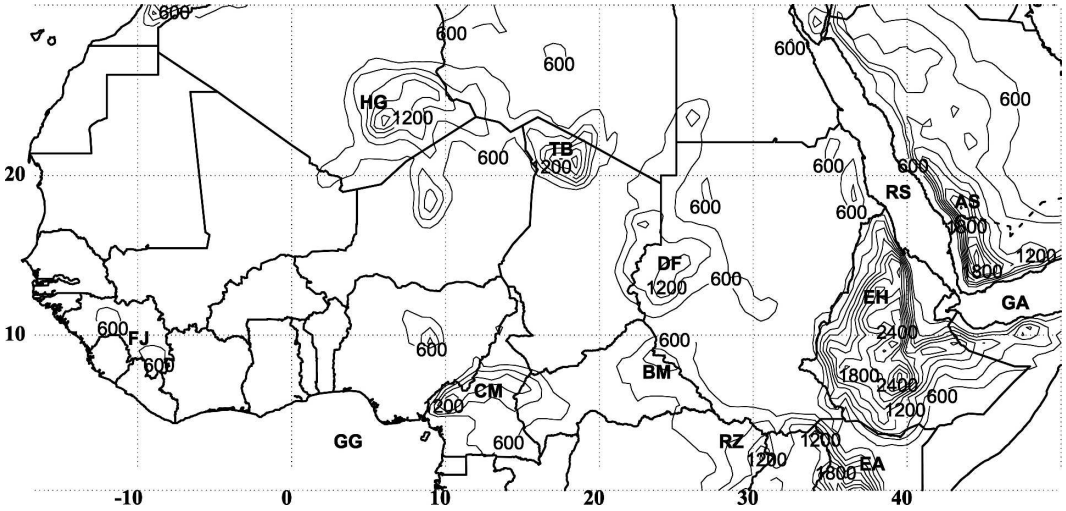

FIG. 1. Terrain data as resolved from ECMWF Operational Model dataset. Terrain is contoured every 200 m. Labels indicate major geographical features of Africa: AS: Asir Mountains; BM: Bongo Massif; CM: Cameroon highlands; DF: Darfur Mountains; EA: Eastern Arc Mountains; EH: Ethiopian highlands; FJ: Futa Jallon highlands; GA: Gulf of Aden; GG: Gulf of Guinea; HG: Hoggar Mountains; RZ: Ruwenzori Mountains; TB: Tibesti Mountains.

mosaic of satellite imagery to demonstrate the existence of westward propagating cloud patterns in a zone from 5° to 15°N. The range of wave periods reported was about 4 to 7 days, while the range of zonal wavelengths was $\lambda = 2000$ to 10 000 km. This wide range in zonal wavelength is attributed to two types of wave modes (Chang et al. 1970). The first mode had a range of $\lambda = 6000$ to 10 000 km and maximum amplitude in the upper troposphere; this mode was categorized as the mixed Rossby–gravity wave mode (Nitta 1970). With a range of $\lambda = 2000$ to 5000 km, the second mode was most prominent in the lower troposphere and was categorized as a forced equatorial Rossby wave mode (Holton 1970, 1971).

The genesis of a lee vortex has been documented to precede an event of tropical cyclogenesis over the eastern Pacific Ocean. A mesovortex (MV) later associated with Hurricane Guillermo (1991) was found to have developed on the lee side of mountains in Central America (Bister and Emanuel 1997; Farfán and Zehnder 1997). This pre-Guillermo MV developed within a preexisting MCC from the interaction of an easterly wave in the Caribbean Sea with the Sierra Madre range of Central America. Mozer and Zehnder (1996) studied analogous lee vortex generation over North Africa. Their idealized numerical simulations produced a barotropically unstable jet from the blocking and channeling of dry, adiabatic, easterly flow between the Hoggar and Atlas Mountains and to the south of the Tibesti Mountains. These barotropically unstable jets contributed to the production of lee vortices and lee troughs downstream of the Hoggar and Tibesti Mountains. The wavelength of these disturbances was roughly 1600 km, and they propagated westward with a period of about 2.5 days, which correspond to values commonly observed with AEWs.

Hurricane Alberto (2000) was traced from an incipient MCC near the Ethiopian highlands (EH) by Hill and Lin (2003). The location of the EH and other major geographical features in Africa are shown in Fig. 1 as resolved by the European Centre for Medium-Range Weather Forecasts (ECMWF) Operational Model (EOM) dataset. Terrain contours of the EH greater than or equal to 1.2-km range approximately 1300 km in the north–south direction and are primarily contained within the range of 35° to 40°E. The Turkana Channel lies to the south of the EH in northern Kenya. Aside from the EH, other significant regions of topography near the 10°N line include the Darfur Mountains (DF), the Cameroon highlands (CM), and the Futa Jallon highlands (FJ). Based on infrared imagery from the *European Meteorological Satellite-7* (*Meteosat-7*), the initial MCC was observed to develop during the afternoon of 28 July 2000 near the EH and to traverse the continent over a 5-day period (Fig. 2) before crossing the Atlantic coastline of Guinea and Sierra Leone on 3 August 2000. A similar development process was found by J. W. Wegiel and C. G. Herbster (2002, personal communication) with Hurricane Luis (1995), which was triggered by an easterly wave. The easterly wave was composed of a mesoscale convective system (MCS) and an MV, each having developed in the vicinity of the EH.

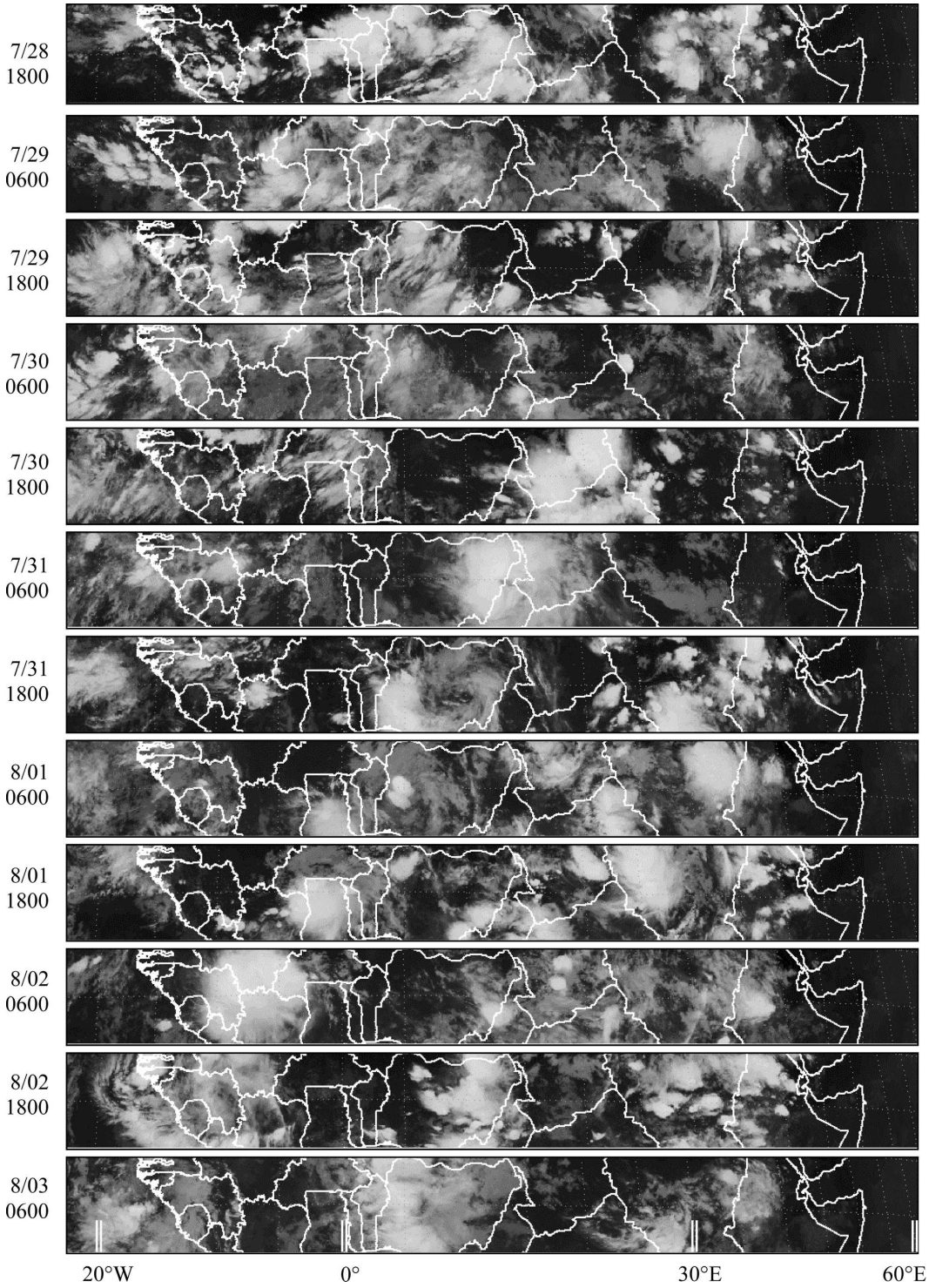

FIG. 2. Time–lon section of *Meteosat-7* infrared satellite imagery for 1800 UTC 28 Jul 2000 through 1800 UTC 3 Aug 2000 every 12 h. Area depicted is approximately 5°–15°N × 25°W–60°E.

Based on our analysis of Meteosat data for the period of 1990 to 2001, 23 of 34 tropical cyclones formed over the eastern Atlantic Ocean (east of 40°W) from disturbances originating from the EH region (Table 1). Therefore, the understanding of the formation mechanisms for these disturbances should be considered important in forecasting the potential formation of tropical cyclones over the eastern Atlantic Ocean. In this

TABLE 1. Tropical cyclones developing (east of 40°W) from MCCs initiated within the area of 5°–15°N × 30°–40°E during the period 1990–2001. Starting times for convection and MCC status are approximated to the nearest third hour UTC based on Meteosat satellite data. MCC status is determined from criteria set by Maddox (1980). Peak classification for each cyclone is defined as follows: TS = tropical storm and H# = hurricane with Saffir–Simpson category of strength. Cyclogenesis positions were determined by the National Hurricane Center.

		Cyclogenesis position					Convection start		MCC start	
Year	Tropical cyclone	Lat (°N)	Lon (°W)	Date	Time (UTC)	Peak classification	Date	Time (UTC)	Date	Time (UTC)
2001	Erin	12.5	34.3	1 Sep	1800	H3	21 Aug	1500	22 Aug	0000
2000	Alberto	10.8	18.0	3 Aug	1800	H3	28 Jul	1200	28 Jul	2100
	Isaac	11.5	23.0	21 Sep	1200	H4	13 Sep	1200	14 Sep	0000
1999	Cindy	13.5	18.9	19 Aug	0000	H4	11 Aug	1200	12 Aug	0000
	Gert	12.6	24.2	11 Sep	1200	H4	4 Sep	1200	5 Sep	0300
1998	Danielle	13.4	34.3	24 Aug	0600	H2	17 Aug	1200	18 Aug	0300
	Ivan	13.4	26.6	19 Sep	0000	H1	10 Sep	1200	10 Sep	1800
	Jeanne	9.6	17.4	21 Sep	0600	H2	15 Sep	1200	15 Sep	1800
1996	Edouard	12.4	19.9	19 Aug	1800	H4	13 Aug	1200	13 Aug	1800
	Gustav	12.7	23.0	26 Aug	0000	TS	19 Aug	0600	19 Aug	1200
	Isidore	8.6	23.3	24 Sep	1200	H3	15 Sep	1200	15 Sep	1800
1995	Felix	14.3	30.8	8 Aug	0000	H4	31 Jul	1200	1 Aug	1800
	Karen	15.4	32.7	26 Aug	1200	TS	17 Aug	1200	18 Aug	0000
	Luis	11.3	22.7	27 Aug	1200	H4	18 Aug	1200	19 Aug	0000
	Pablo	8.3	31.4	4 Oct	1800	TS	25 Sep	1200	25 Sep	1800
1994	Chris	11.3	39.4	16 Aug	1200	H1	6 Aug	1200	7 Aug	0000
	Ernesto	10.1	29.9	21 Sep	1800	TS	8 Sep	1200	9 Sep	0000
1993	Dennis	13.6	30.8	23 Aug	1200	TS	13 Aug	1200	13 Aug	1800
1992	Andrew	10.8	35.5	16 Aug	1800	H4	7 Aug	1200	7 Aug	1800
1991	Danny	10.4	25.8	7 Sep	0000	TS	26 Aug	1200	26 Aug	1800
1990	Hortense	12.5	35.0	25 Aug	0000	TS	15 Aug	1200	16 Aug	0000
	Isidore	7.2	23.4	4 Sep	0000	H2	27 Aug	1200	27 Aug	1800
	Josephine	14.0	32.0	21 Sep	0600	H1	9 Sep	1200	9 Sep	1800

study, we further substantiate that the pre-Alberto disturbance originates from the EH region and test a hypothesis that the pre-Alberto disturbance developed within, and propagated with, an AEW train.

Hodges and Thorncroft (1997, hereafter HT97) utilized Meteosat imagery and ECMWF reanalysis data to produce an 8-yr (1983–90) climatology of African MCCs. Many of the African MCCs tended to develop near regions with high topography. One such region identified was the EH, where African MCCs most often developed during the months of July and August of the 8-yr climatology study. This climatological study concluded that most MCCs originating near the EH tend to track southwestward and dissipate in a so-called lysis region before the completion of one diurnal cycle. Given the lack of direct, in situ observations throughout North Africa, satellite imagery is a highly valuable resource for detecting African MCC development and propagation, and the inference of underlying disturbances contributing to the initiation and sustenance of the MCCs. While the individual MCCs can be traced only during a relatively short lifespan, the associated disturbances can be identified through interpolation of the MCC positions and the trace of the residual, propagating cloud elements. Here, we partially adopt the methodology of HT97 by analyzing the pre-Alberto disturbance with Meteosat imagery and EOM data, categorize periods (as opposed to quasi-instantaneous events) of convective genesis and lysis into stages, and show how the pre-Alberto disturbance can be identified within a cycle of convective genesis and lysis. In fact, Berry and Thorncroft (2005) confirmed much of the satellite chronology alluded to by Hill and Lin (2003) for the beginnings of Hurricane Alberto, specifically from the DF of Sudan westward, and analyzed the evolution of the AEW over West Africa with EOM data and synoptic observations. In this study, we provide further evidence that the pre-Alberto disturbance, consisting of an incipient MCC and an MV, is embedded within an AEW that concurrently develops downstream of the EH, as proposed by Hill and Lin (2003). As the reliability of ECMWF analyses to resolve mesoscale features over northern Africa could be considered questionable, we employ a mesoscale-resolving numerical model to simulate the potentially formative environment of the AEW over the span of North Africa.

Section 2 presents more detailed evidence of the ori-

TABLE 2. Convective cycle of the pre-Alberto MCCs. Initiation and dissipation times are estimated to the nearest hour UTC; TD = beginning of tropical depression.

Convective cycle	Initiation time*	Dissipation time*	Stage duration (h)	Approximate track locations
Genesis I (G-I)	1000 UTC 28 Jul	0800 UTC 29 Jul	22	(13.0°N, 39.0°E) to (12.5°N, 33.0°E)
Lysis I (L-I)	0800 UTC 29 Jul	0200 UTC 30 Jul	18	(12.5°N, 33.0°E) to (12.5°N, 28.0°E)
Genesis (G-II)	0200 UTC 30 Jul	1400 UTC 31 Jul	34	(12.5°N, 28.0°E) to (10.0°N, 12.0°E)
Lysis II (L-II)	1400 UTC 31 Jul	0200 UTC 1 Aug	12	(10.0°N, 12.0°E) to (10.0°N, 7.5°E)
Genesis III (G-III)	0200 UTC 1 Aug	1200 UTC 2 Aug	34	(10.0°N, 7.5°E) to (10.0°N, 8.0°W)
Lysis III (L-III)	1200 UTC 2 Aug	1000 UTC 3 Aug	22	(10.0°N, 8.0°W) to (10.0°N, 16.0°W)
Genesis IV (G-IV)	1000 UTC 3 Aug	0900 UTC 4 Aug (TD)	23	

* Time estimated to the nearest hour UTC.

gin and convective cycle of the pre-Alberto MCCs from the lee of the EH into a tropical cyclone, while section 3 describes the origin and propagation of an AEW-like, pre-Alberto disturbance. Details of the numerical model, experiment design, and simulation of the formation and maintenance of an easterly wave and associated MCCs and MV are presented in section 4. Concluding remarks are featured in section 5.

2. Convective cycle of the pre-Alberto disturbance

a. Trace of pre-Alberto disturbance using Meteosat-7 *data*

The track of the pre-Alberto disturbance was previously analyzed by Hill and Lin (2003) using *Meteosat-7* satellite imagery. Our present study uses infrared-wavelength (IR) data of 5-km resolution to confirm the entire track of pre-Alberto MCCs over the African continent. Time periods of convective genesis and lysis are estimated, as are the times when MCC criteria (given by Maddox 1980) have been satisfied. Given that MCCs are generally circular in nature, we measured the zonal and meridional axes of each pre-Alberto MCC, and then estimated the coverage area of the MCCs.

Figure 2 shows the time–longitude section of *Meteosat-7* IR imagery from 1800 UTC 28 July 2000 to 1800 UTC 3 August 2000 every 12 h. Hill and Lin (2003) noted that no moist convection was evident before 1000 UTC (1300 local time) 28 July over the EH. It is further noted here that no moist convection was evident over the EH, the Horn of Africa, the Red Sea, the Arabian Peninsula, or the Arabian Sea during the period of 2100 UTC 27 July to 1000 UTC 28 July (not shown). By 1800 UTC 28 July (Fig. 2), convective clouds cover much of the EH region. By 0600 UTC 29 July, the convection has already peaked as an MCC and has begun to dissipate. At about 0830 UTC 29 July, the first lysis stage, L-I, is determined to begin (Table 2; Fig. 3b). The residual MV of the MCC propagates to a central position of approximately 30°E. The new proximity of the MV circulation to the Sahara Desert suggests that the entrainment of low-level dry air may have led to the disruption of convection. New convection develops with the pre-Alberto disturbance between the DF of Sudan and the Bongo Massif (BM) of the Central African Republic at about 0200 UTC 30 July, beginning the second genesis (G-II) stage (Table 2; Fig. 3b). A reactivated MCC is observed at 1800 UTC 30 July (Fig. 2), and the MCC expands to a peak area of about 6×10^5 km^2 over southern Chad and the Central African Republic (Fig. 3b).

After 1400 UTC 31 July, the MCC begins to dissipate north of the CM, thus ending the G-II stage and starting the second lysis (L-II) stage. The presence of the Cameroon highlands may have disrupted the inflow of moisture to the MV and disrupted the associated convection during this lysis stage, rendering the MV circulation visible (Fig. 2). The L-II stage lasts for approximately 12 h before more convection develops at approximately 0200 UTC 1 August, beginning the third genesis stage (G-III). The MCC is firmly reestablished by 0000 UTC 2 August, and this third MCC is observed to flourish over western Africa around 10°N (Fig. 2), where the terrain is generally flat. The third lysis stage (L-III) begins after 1200 UTC 2 August as the pre-Alberto disturbance approaches the FJ. No additional MCC redevelopment occurs with the pre-Alberto disturbance as it propagates westward across the Atlantic coast of Guinea and Sierra Leone at approximately 0000 UTC 3 August (Figs. 2 and 3). The precyclogenic MCC is established after 0600 UTC 3 August over the eastern Atlantic Ocean (Fig. 2).

The trace of the pre-Alberto disturbance ends with the cyclogenesis stage at 1800 UTC 3 August. The complete track of the pre-Alberto disturbance is sketched in Fig. 3a with genesis and lysis stages denoted. In summary, the pre-Alberto disturbance traveled from 37°E

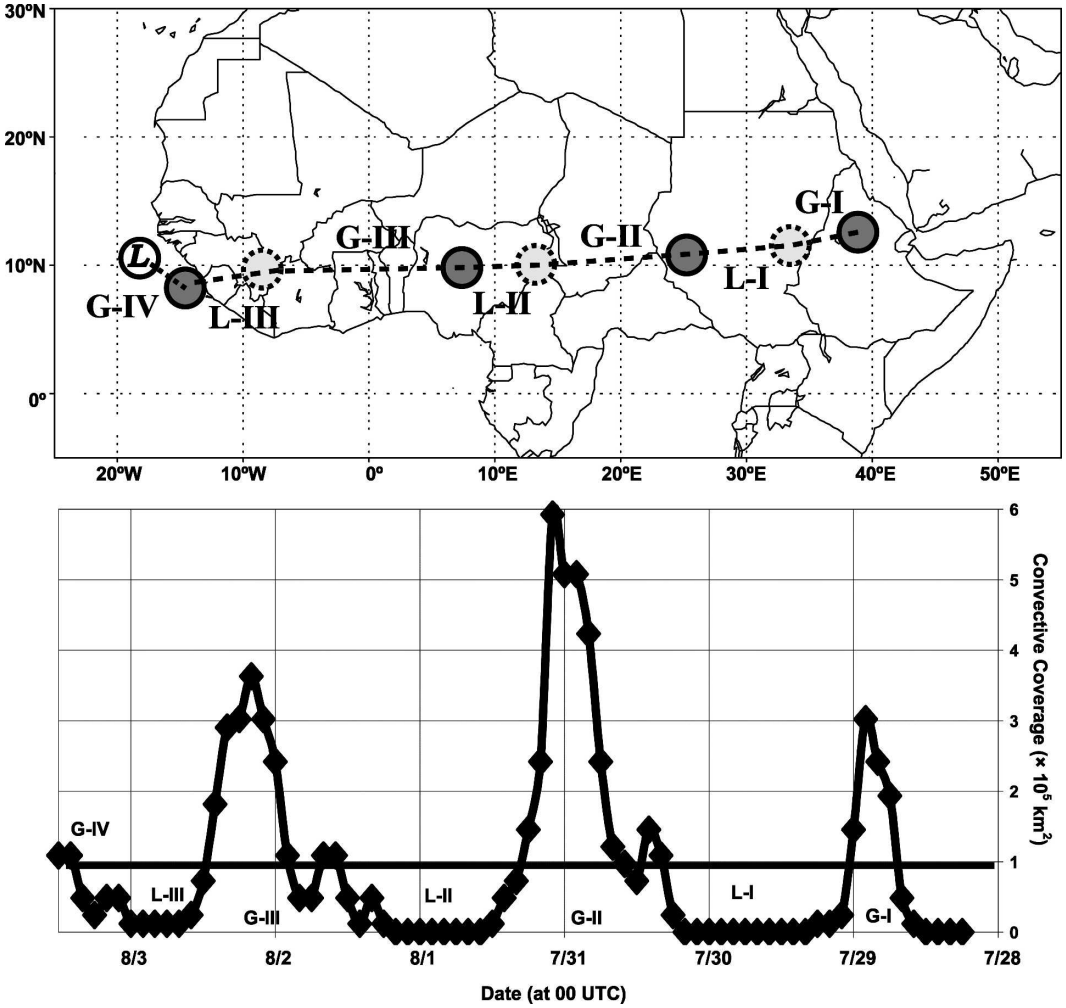

FIG. 3. (a) Track of pre-Alberto MCCs estimated from *Meteosat-7* satellite imagery, with genesis (G-I, G-II, G-III, and G-IV) and lysis (L-I, L-II, and L-III) stages denoted, and (b) convective cloud coverage area of pre-Alberto MCC. The horizontal bold line in (b) is the threshold for MCC designation. The definitions of the genesis and lysis stages are listed in Table 2.

to 18°W over a period of approximately 6 days with an average propagation speed of 11.6 m s^{-1}.

b. Trace of pre-Alberto disturbance using ECMWF Operational Model data

We examined 6-hourly fields of vertical velocity, relative vorticity, and water vapor mixing ratio from EOM analysis data to identify the pre-Alberto disturbance. The EOM data were translated from a T213 spectral grid to a grid of 0.5° spatial resolution over a rectangular area of approximately (5°–15°N) × (25°W–60°E). For space considerations, 12-hourly plots of EOM data are presented here.

Figure 4 shows the time evolution of 700-hPa vertical velocity ($\omega \leq -10^{-3}$ hPa s^{-1}) over North Africa starting on 1800 UTC 28 July 2000. A region of significant upward air motion is collocated over the northern EH with developing moist convection (Figs. 2 and 4). The region of upward motion propagates with the first pre-Alberto MCC (and the pre-Alberto disturbance) over Sudan by 0600 UTC 29 July. The concentrated upward motion region becomes diffuse by 1800 UTC 29 July, during the L-I stage, and is not discernable again until 1800 UTC 30 July, during the G-II stage (Table 2; Figs. 3 and 4). On 0600 UTC 31 July, immediately after the convective peak of the second pre-Alberto MCC, the upward motion region has redeveloped and is roughly collocated with convection over northeast Nigeria. After the second pre-Alberto MCC has diminished, the upward motion region is positioned near the observed MV at 1800 UTC 31 July (Figs. 2 and 4). At the 700-hPa

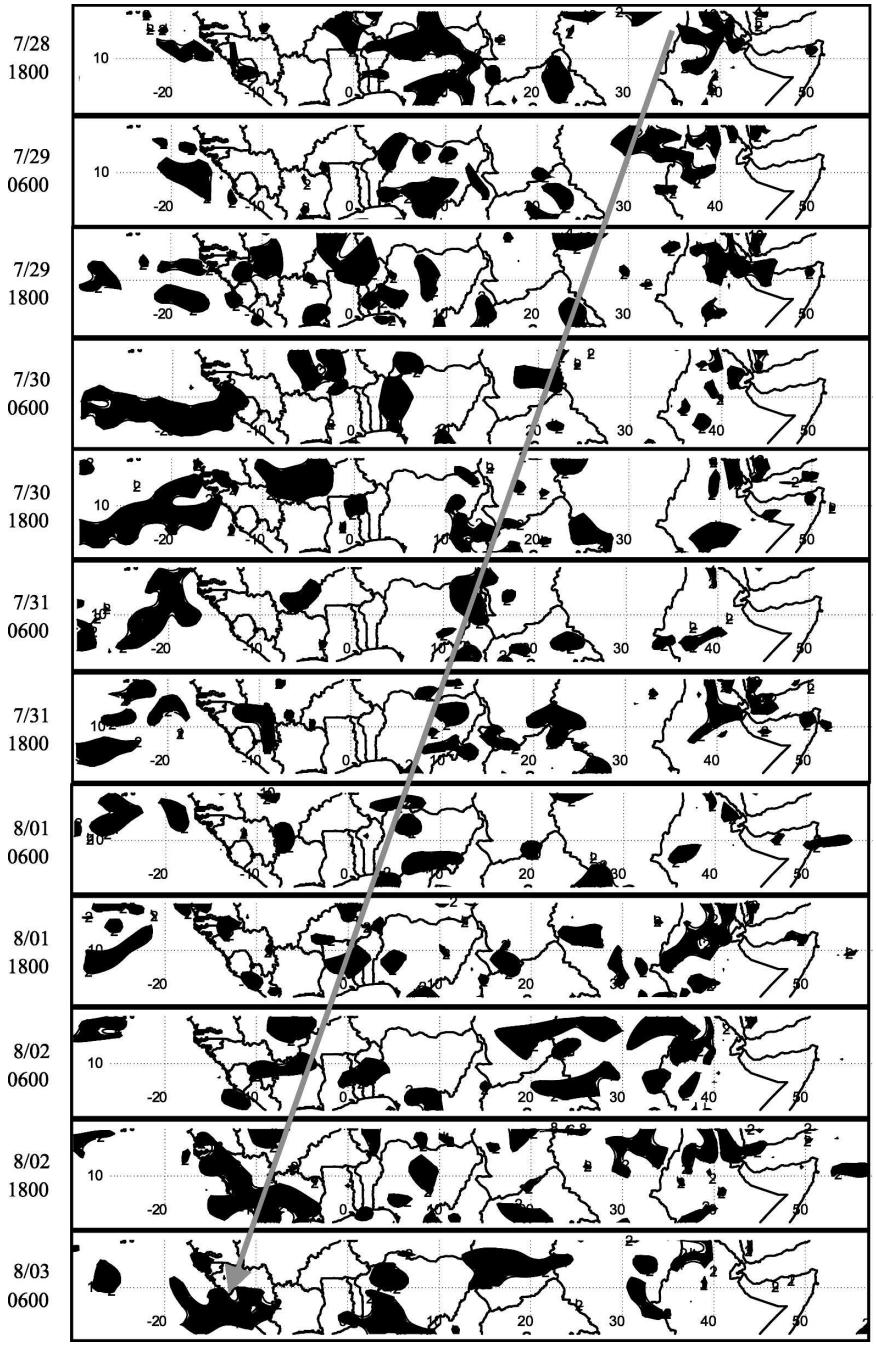

FIG. 4. EOM 700-hPa vertical velocity (ω) field for 1800 UTC 28 Jul–0600 UTC 3 Aug 2000 every 12 h. Regions of $\omega \leq -10^{-3}$ hPa s^{-1} are shaded. Arrow indicates approximate track of anomaly associated with the pre-Alberto disturbance.

level (Fig. 4) and the 500-hPa level (not shown), the upward motion region of interest propagates westward with the pre-Alberto disturbance from 0600 UTC 1 August through 1800 UTC 2 August to the Atlantic coast. The region of the upward motion expands as the pre-Alberto disturbance crosses the coastline, although no new MCC redevelopment occurs until 1200 UTC 3 August.

The EOM 700-hPa relative vorticity field ($\geq 10^{-5}$ s^{-1}) most clearly shows the pre-Alberto disturbance after 1800 UTC 31 July (Fig. 5). Before this time, however, no concentrated area of significant cyclonic vor-

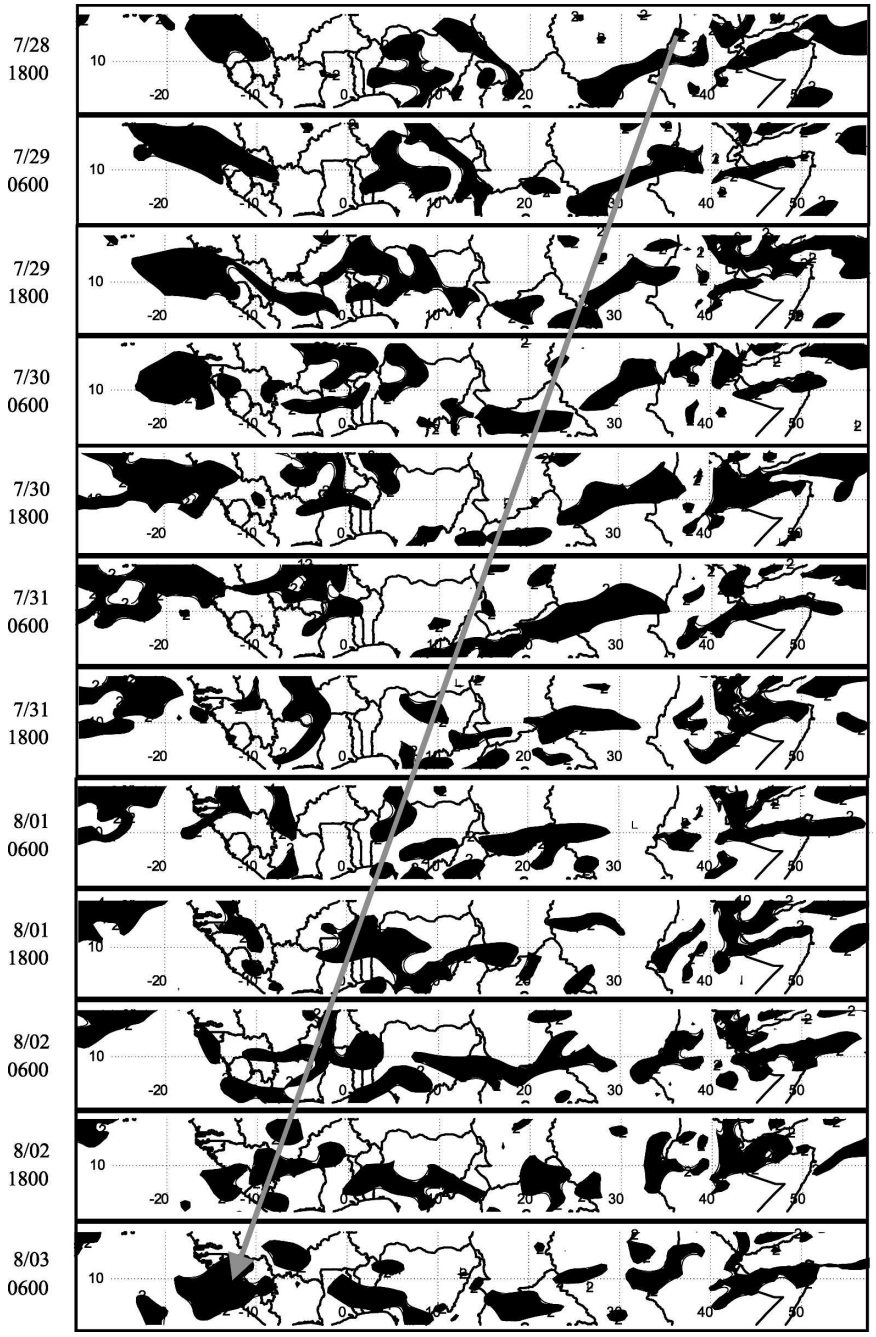

FIG. 5. Same as Fig. 4 except for 700-hPa relative vorticity. Regions of $\zeta \geq 10^{-5}$ s^{-1} are shaded.

ticity can be identified with the pre-Alberto disturbance. The disturbance is less discernable within the 500-hPa relative vorticity field (not shown), indicating that the disturbance is steered and partially maintained by the African easterly jet near the 700-hPa level, which is consistent with observations (e.g., Thorncroft and Hoskins 1995). The cyclonic vorticity signal observed in satellite imagery is diminished in the EOM data, likely a result of the assimilation of the sparse observation network and of an insufficiency in the EOM data to resolve the observed vorticity signal. The employment of a mesoscale numerical model would be needed to obtain a more detailed representation of the pre-Alberto disturbance.

The pre-Alberto disturbance is best represented by the EOM 700-hPa water vapor mixing ratio field (Fig. 6). Throughout the presented time series abundant moisture ($\geq$8 g kg^{-1}) is present over, and in the vicinity of, the EH. A solitary region of high moisture propagates westward from the EH region after 1800 UTC 28 July, closely following the satellite track of the pre-Alberto disturbance. The total area covered by this propagating high moisture region fluctuates with the observed stages of convective genesis and lysis. The high moisture region covers the least area during the L-I stage, and the greatest area during the G-II stage (Figs. 3 and 6).

To better establish the importance of water vapor availability to this case, we analyze the National Centers for Environmental Prediction (NCEP) mean surface relative humidity, $\overline{\text{RH}}$, over the African continent for July and August 2000 (Fig. 7). In general, there are four areas of $\overline{\text{RH}} \geq 90\%$ over the African continent along 10°N, the latitude most closely followed by the pre-Alberto disturbance. These four areas of high $\overline{\text{RH}}$ are roughly located at about 37°E, 23°E, 10°E, and 8°W (Fig. 7), with regions of significant topography (Fig. 1). The Lysis-I (~32°E) and Lysis-II (12°E) regions roughly coincided with areas of relatively low $\overline{\text{RH}}$ along 10°N (Figs. 3a and 7). Hence, *the availability of water vapor is the most essential factor controlling the convective cycle of the pre-Alberto disturbance over the African continent*, *and the presence of significant topography contributes to the generation or decay of the associated MCCs through regulation of the water vapor supply.* A more rigorous climatological study and a detailed numerical study will be needed to further substantiate the importance of water vapor supply to the maintenance of the pre-Alberto disturbance and its associated MCCs; these studies will be presented in our future work.

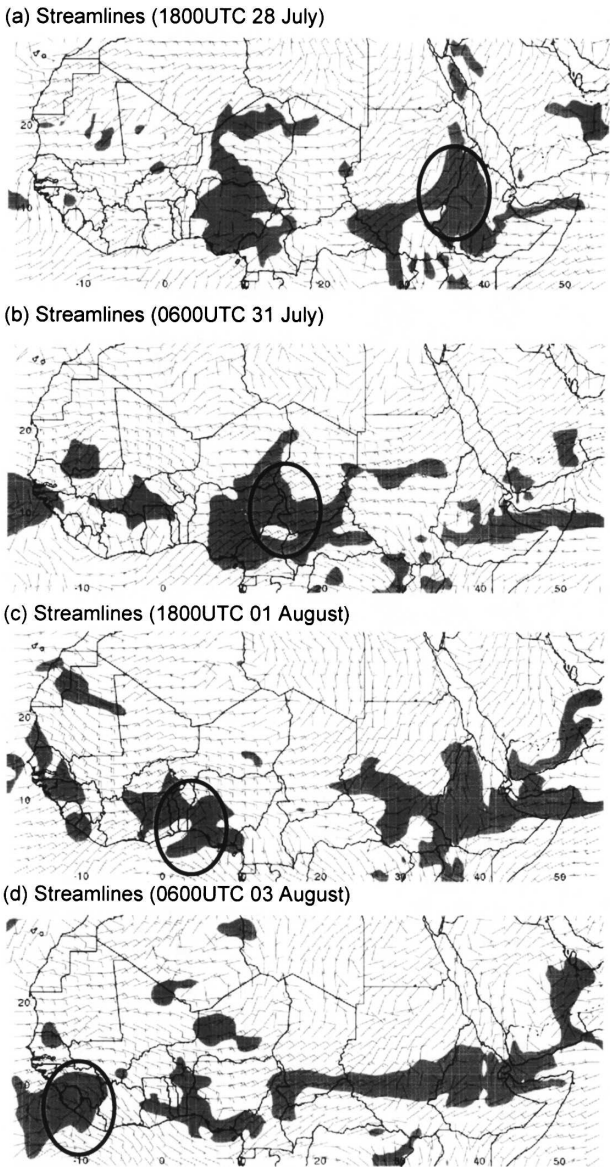

FIG. 6. EOM 700-hPa mixing ratio and vector wind at (a) 1800 UTC 28 Jul, (b) 0600 UTC 31 Jul, (c) 1800 UTC 1 Aug, and (d) 0600 UTC 3 Aug 2000. Regions with mixing ratio values greater than 8 g kg^{-1} are shaded.

3. Origin and propagation of the AEW associated with the pre-Alberto disturbance

The pre-Alberto disturbance most likely originated from the EH because no signature of this disturbance was discernable east of the EH from the *Meteosat-7* imagery (Fig. 2) and from EOM vertical velocity fields (Fig. 4). The synoptic environment of the G-I period has been described in Hill and Lin (2003). Based on the satellite data, other MCSs existed ahead of and behind the westward propagating pre-Alberto MCC over North Africa during our period of study. The MCSs east of the pre-Alberto MCC similarly developed in the vicinity of the EH, while a cycle of convective genesis and lysis was observed with the MCSs west of the pre-Alberto MCC (Fig. 2). EOM analysis data reveal a semblance of an AEW train (Figs. 4–6) superposed with the satellite positions of the MCSs.

At the EH, there exist two modes of disturbance development: a stationary mode and a propagating mode. The stationary mode corresponds with the generation of moist convection over the EH triggered by diurnally variant sensible heating over the mountains. The propagating mode corresponds with the generation and propagation of MVs and MCSs from the lee side of the EH over a period of about 2 to 3 days, which we

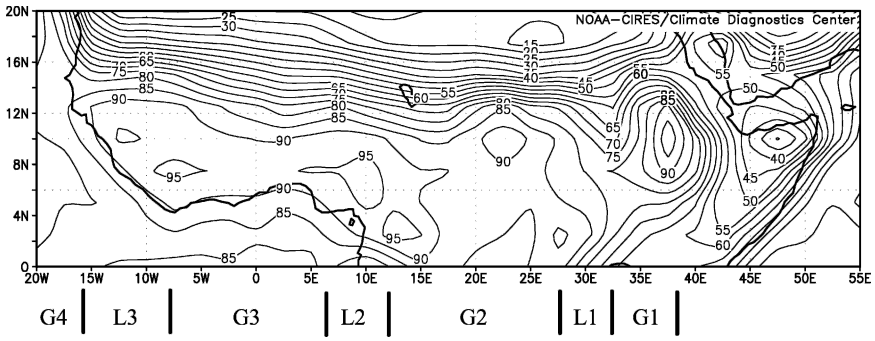

FIG. 7. Mean relative humidity ($\overline{RH}$) for Jul and Aug 2000 over North Africa from NCEP reanalysis data. Genesis and lysis stages of the pre-Alberto MCCs are labeled at the bottom.

identify here at 0600 UTC 29 July, 0600 UTC 1 August, and 0600 UTC 3 August (Figs. 2 and 4–6). The collective disturbance propagates westward (downstream) across the African continent at an average speed of 11.6 m s^{-1}. The wavelength between the disturbances is roughly estimated to be about 2200 km. Previous observational analyses report that AEWs typically have a period of 3–5 days, a wavelength of 2000–4000 km, and propagate westward with a mean speed of 7–9 m s^{-1} (6°–7° longitude per day) at mean latitude of 11°N (e.g., Reed et al. 1977). The wave train depicted by Meteosat data, and emulated by EOM analyses, closely matches the AEW classification.

The 700-hPa EOM wind vector fields for 1800 UTC 28 July, 0600 UTC 31 July, 1800 UTC 1 August, and 0600 UTC 3 August are shown in Fig. 6. Throughout the time series presented southwesterly flow exists to the west of the EH region, particularly below the 700-hPa level (not shown), and southeasterly flow runs through the Turkana Channel to south of the EH region. The advection of moisture to the EH region from the southwesterly flow, and to a lesser extent from the Turkana Channel flow, largely contribute to the high surface $\overline{RH}$ exhibited in Fig. 7. In turn, the presence of abundant moisture near the sensibly heated EH surface would lead to regular convective development during the period of July–August 2000 (not shown). Convection already present on 1800 UTC 28 July would have continued to draw moisture advected to the west slopes of the EH by southwesterly and southeasterly flow (Fig. 6a). The cyclonic vortex depicted near 8°N, 30°E could be a manifestation, resolved within the EOM data, of a vortex that developed in a manner similar to the pre-Alberto MV described by Hill and Lin (2003). The vortex near 18°N, 32°E could be a product of horizontal shear over northeastern Sudan. Farther to the west, there was a region of strong convergence and cyclonic flow at about 11°N, 8°E, which likely represents an AEW perhaps 3 days removed from the EH. At 0600 UTC 31 July (Fig. 6b), the region of cyclonic, convergent flow located near 10°N, 12°E coincides with the position of the pre-Alberto disturbance. A separate AEW with an apparent vortex is positioned near 13°N, 4°W. The continued moist-advective flow near the EH region, meanwhile, would contribute to the later formation of a new MCC at 0600 UTC 31 July (Figs. 2 and 6b). For 1800 UTC 1 August (Fig. 6c), the pre-Alberto disturbance is depicted as an area of convergence within a broad cyclonic circulation near 10°N, 5°W. As noted previously, the EOM data are not capable of fully resolving the pre-Alberto disturbance, particularly the associated MV. At 0600 UTC 3 August, the pre-Alberto system can be observed near 9°N, 12°W exiting the North African region and emerging over the eastern Atlantic Ocean (Fig. 6d).

Cross-sectional analyses of EOM meridional wind data along 10°N present an alternative perspective of AEW activity over North Africa (Fig. 8). The times of these cross-sectional analyses were chosen to show AEW signals along 10°N during the lifespan of the pre-Alberto disturbance. At each given time, one can identify two or three waves across the African continent. On 1800 UTC 28 July, northerly–southerly flow couplets at 5° and 33°E identify AEW locations (Fig. 8a). The northerly–southerly flow couplet at 5°E is based primarily in the lower troposphere, below the 700-hPa level. The northerly–southerly flow couplet at 33°E is based within the middle troposphere, between the levels of 700 and 500 hPa, owing to the dominating presence of the EH in the lower troposphere. Some semblance of the pre-Alberto disturbance can be, at best, construed from the weak northerly–southerly flow couplets at 38°E. On 1800 UTC 31 July, northerly–southerly flow couplets are situated at 5°W and 27°E (Fig. 8b). At this time, the pre-Alberto disturbance is weakly represented at 8°E with shallow, northerly flow. On 0600 UTC 2 August, the pre-Alberto disturbance is represented by a vertically disjointed northerly–

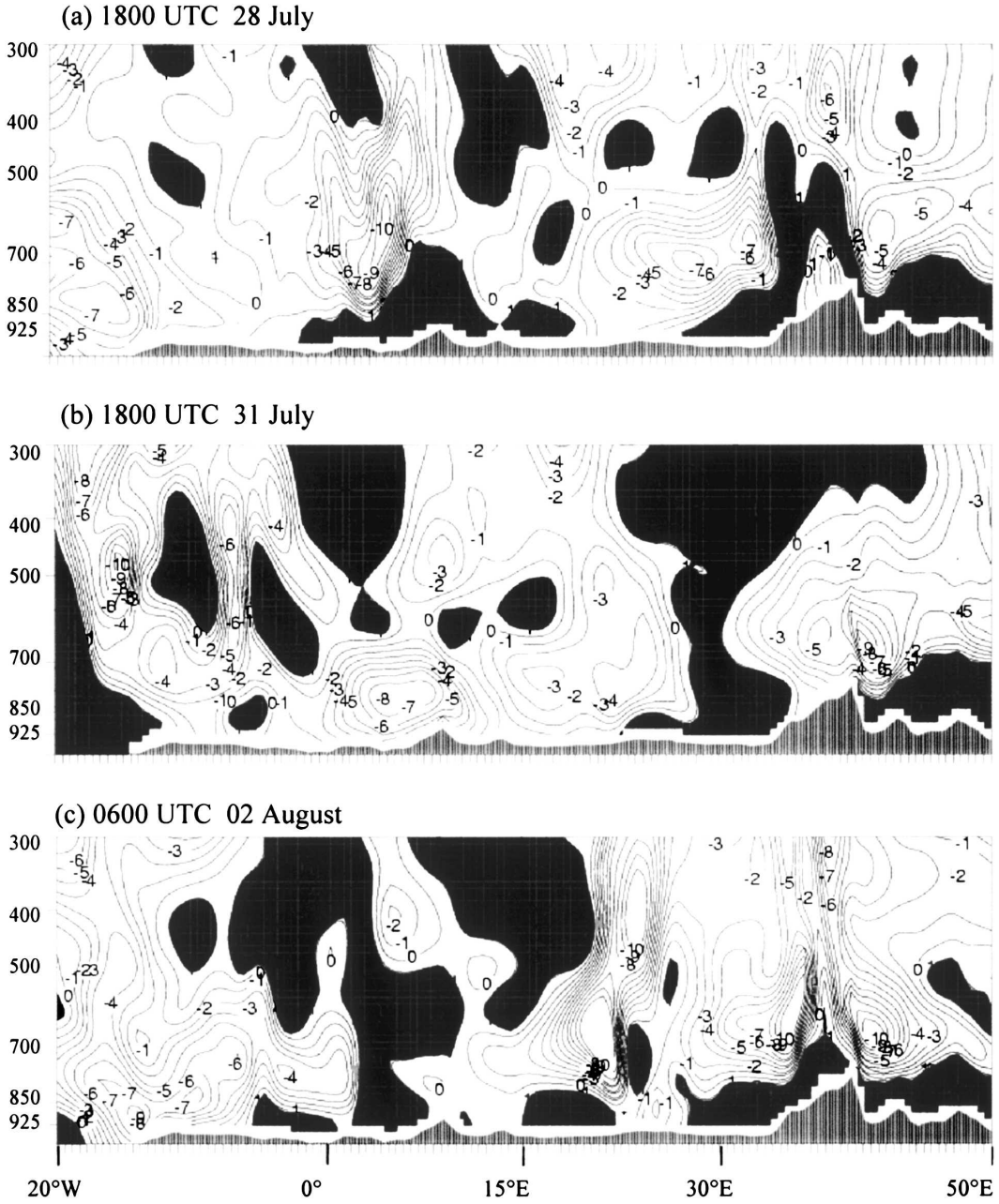

FIG. 8. Vertical cross section of EOM meridional wind (v) fields at 10°N for 1800 UTC for (a) 28 Jul 2000, (b) 31 Jul 2000, and (c) 1 Aug 2000. Areas of $v \geq 1$ m s^{-1} are shaded, while northerly wind velocities are contoured every 1 m s^{-1}. The y axis is pressure in hPa.

southerly flow couplet at 5°W (Fig. 8c), with the northerly–southerly flow couplet reflected at the 925- and 600-hPa levels, but not between these levels. Other northerly–southerly flow couplets are located at 22° and 35°E. Compared with the 700-hPa vorticity field (Fig. 5), the added dimension of height more clearly reveals the evolution of the pre-Alberto disturbance west of 15°E. Despite the complexities of the vertical meridional wind field, AEW signals are identified at similar longitudinal positions to signals within the horizontal fields (Figs. 4–6). Wave activity tends to be more evident over West Africa, due to a more abundant moisture supply (Figs. 6 and 7), stronger baroclinicity over the Sahel, and reduced frictional braking of low-level wind nearer the relatively flat coastal regions.

AEW signals are also reflected in the cross-sectional

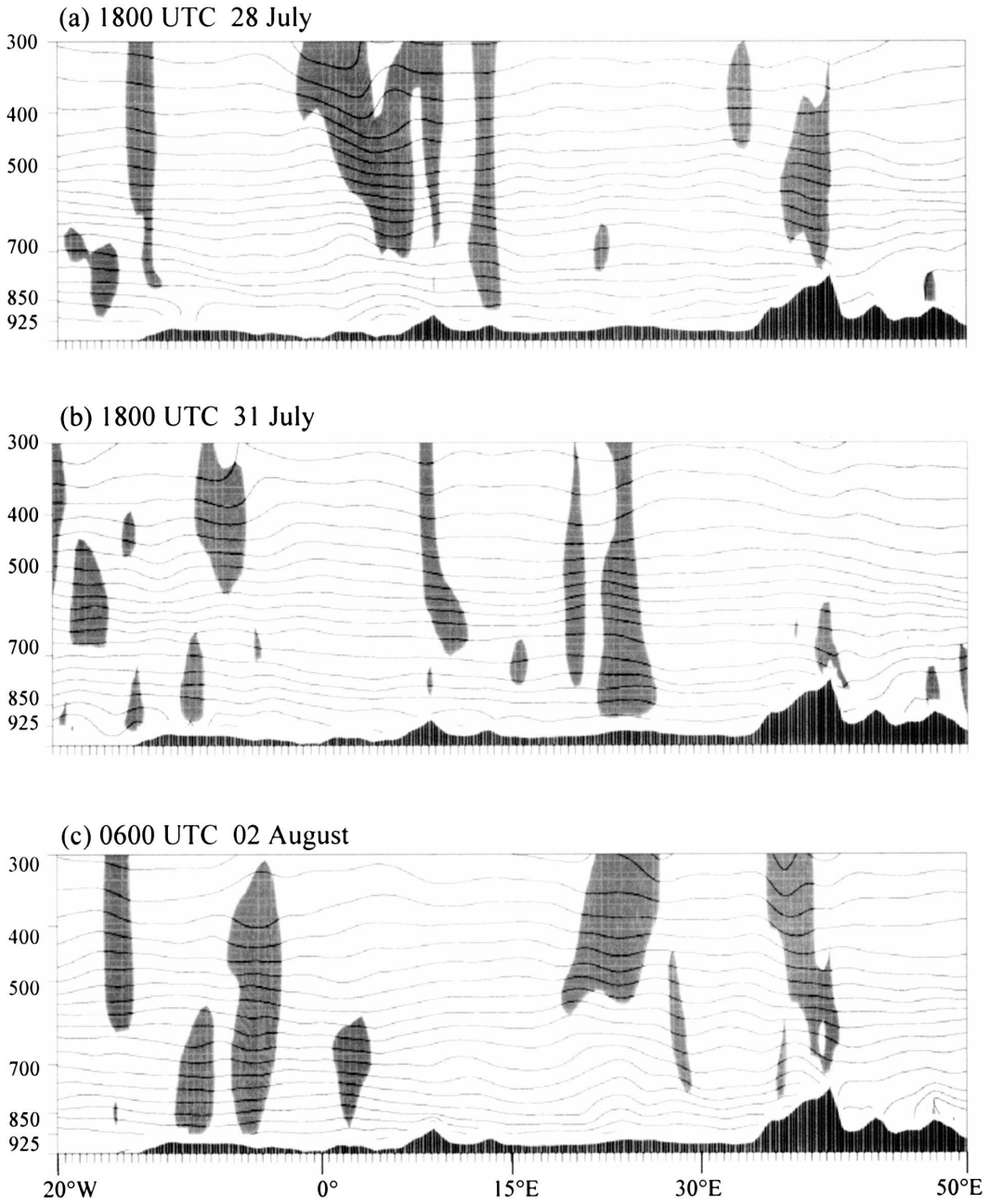

FIG. 9. Same as Fig. 8 except for vertical velocity (ω) and potential temperature (θ) fields. Regions of $\omega \leq -10^{-3}$ hPa s^{-1} are shaded; θ is contoured every 2 K.

fields of vertical velocity and, to a lesser degree, potential temperature (Fig. 9). Regions where $\omega < -10^{-3}$ hPa s^{-1} are juxtaposed in horizontal space with each of the northerly–southerly flow couplets identified in the meridional wind fields (Fig. 8), including the weak signal of the pre-Alberto disturbance on 1800 UTC 31 July (Fig. 9b). Despite the lack of vertical contiguity with the northerly–southerly flow couplets at 5°W on 0600 UTC 2 August, upward air motion is shown to be present throughout the layer of 925–300 hPa (Fig. 9c) at this location and time. Regions of $\omega < -10^{-3}$ hPa s^{-1} exhibit no appreciable vertical phase tilt, indicating that upward air motion along 10°N is modulated primarily by convection. The only consistent region of $\partial\theta/\partial x > 0$ is over the EH, especially with the development of an AEW (Figs. 8a and 8c).

In summary, we found that the pre-Alberto disturbance exhibited characteristics of an AEW. Analyses of

EOM data, in conjunction with analysis of Meteosat data, show that this AEW originated from the EH, as there were no discernable signals of AEW activity east of the EH region prior to the development of the first MCC. In the next section, we use a numerical simulation to demonstrate how AEWs and MVs may develop through orographic effects.

4. Numerical simulation of the formation and propagation of easterly waves and MVs

a. Model specifications and experiment design

The National Center for Atmospheric Research (NCAR) Regional Climate Model Version 3.0 (henceforth RegCM3) is used to further our understanding of the formation and maintenance of the AEW associated with the pre-Alberto system from 2000. The RegCM3 is relatively simple in comparison to other numerical weather prediction models and is less computationally expensive. The RegCM3 was chosen for this specific case to allow for a larger domain and some important physical processes, such as planetary boundary layer processes and latent heating, to be included into the simulations at a reasonably fine grid resolution (i.e., 30 km). These specifications will allow us to simulate the synoptic-scale environmental conditions surrounding and associated with the AEW present during the pre-Alberto period.

The RegCM3 is a three-dimensional, hydrostatic, compressible, finite-difference model with vertical σ coordinates and has the following characteristics:

- Arakawa–Lamb B-staggering horizontal grid calculated using velocity variables with respect to the scalar variables
- Relaxation (exponential) lateral boundary conditions
- Biosphere–Atmosphere Transfer Scheme (BATS1E) surface physics as described by Dickinson et al. (1993)
- Nonlocal planetary boundary layer scheme as described by Holtslag et al. (1990)
- Grell (1993) cumulus parameterization scheme implementing the Fritsch and Chappell (1980) closure assumptions
- Zeng et al. (1998) ocean flux parameterization scheme
- Subgrid explicit moisture scheme (SUBEX) large-scale precipitation scheme (Pal et al. 2000).

The NCEP 2.5° reanalysis data are used for model initialization and updated boundary conditions during the model integration. The sea surface temperature (SST) fields were initialized from the National Oceanic and Atmospheric Administration (NOAA) optimum interpolation sea surface temperature (OISST) 1° datasets. Topographical data were obtained from the GTOPO30 global digital elevation model (DEM) at a 10-min resolution.

The model specifications used in the real case control run are as follows: 1) 30-km resolution, 18 σ levels (0, 0.05, 0.1, 0.16, 0.23, 0.31, 0.39, 0.47, 0.55, 0.63, 0.71, 0.78, 084, 0.89, 0.93, 0.96, 0.98, 0.99, and 1.0); 2) the domain covers the entirety of the North African continent from 5°S to 25°N and 25°W to 60°E, centered at about 10°N, 17.5°E and composed of 312 $\times$ 110 horizontal grid points; (3) 60-s time interval; and (4) 14-day (or 336 h) simulation time starting on 1200 UTC 20 July 2000 and ending 1200 UTC 3 August 2000.

b. Formation and propagation of easterly waves and MVs from the RegCM3 real case simulation

In this section we discuss the results of the RegCM3 30-km real case simulation. Since the model was initialized at 1200 UTC 20 July 2000, it provided an 8-day period for the model to spin up before the onset of the pre-Alberto system on the lee side of the EH at 1000 UTC 28 July 2000. The relative vorticity field at 700 hPa is shown at a 12-h interval from 1800 UTC 28 July to 0600 UTC 3 August in Fig. 10. As in section 2, the line drawn indicates where the pre-Alberto system is roughly located during that time period as detected in the IR satellite imagery (Fig. 2). The field of relative vorticity shows a clear signal of the pre-Alberto system from 1800 UTC 28 July through 0600 UTC 3 August. From 0600 UTC 29 July, during the extreme latter part of the G-I convectively active stage, through 1800 UTC 29 July, the middle of the L-I convectively dormant stage, the relative vorticity shows a weak and unorganized pre-Alberto system, but the signal was observed to be present (refer to Table 2 for convective periods). From 0600 UTC 30 July through 1800 UTC 1 August, from the G-II period to the G-III period, the relative vorticity indicates the presence of an organized system tracking westward (Fig. 10). At 0600 UTC 2 August, the relative vorticity weakens and becomes less organized, in conjunction with the L-III convective period. The system reorganizes and strengthens at 0600 UTC 3 August when the pre-Alberto system reforms in the G-IV stage. The propagating wave mode, associated with the westward progression of the AEW, and the stationary mountain-induced wave mode, located at about 40°E near the EH region, are both evident in the relative vorticity field (Fig. 10).

Simulated AEW characteristics can also be deduced

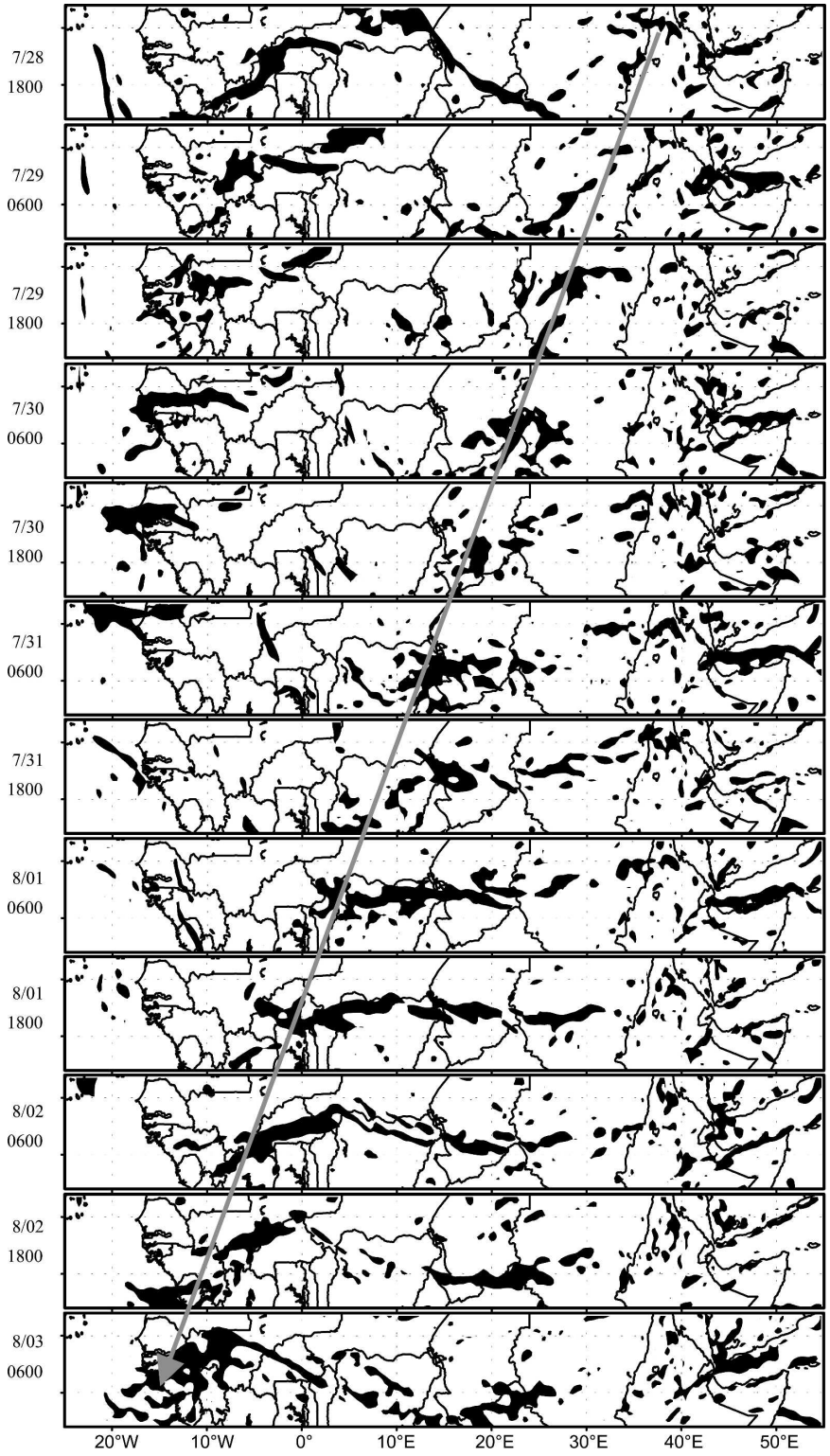

FIG. 10. Relative vorticity at the 700-hPa level, from the RegCM3 30-km control case simulation, with the region of $\zeta \geq 10^{-5}$ s^{-1} shaded.

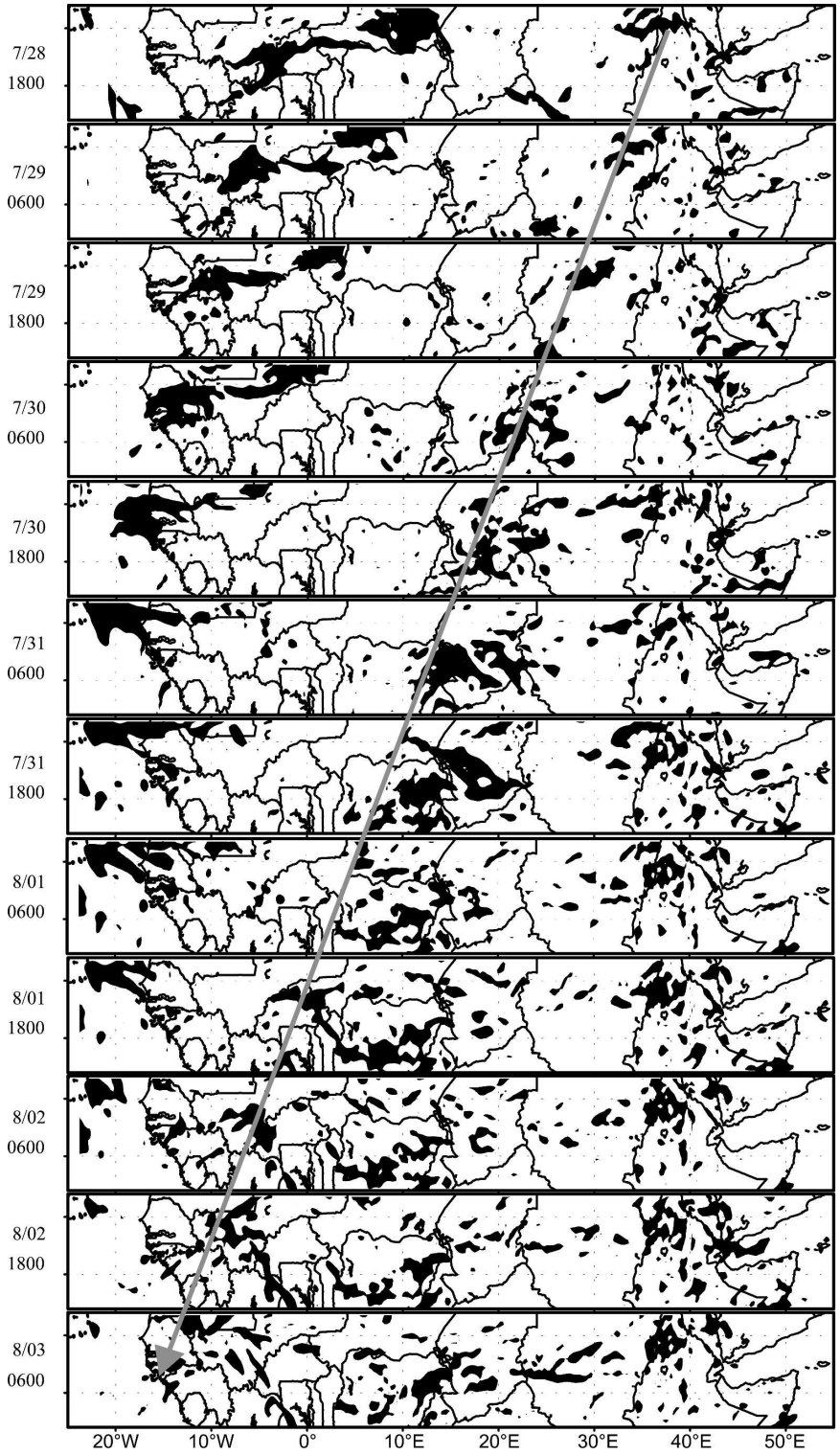

FIG. 11. Potential vorticity at the 700-hPa level, from the RegCM3 30-km control case simulation, with the region of PV $\geq 4 \times 10^{-7}$ K m^2 s^{-1} kg^{-1} shaded.

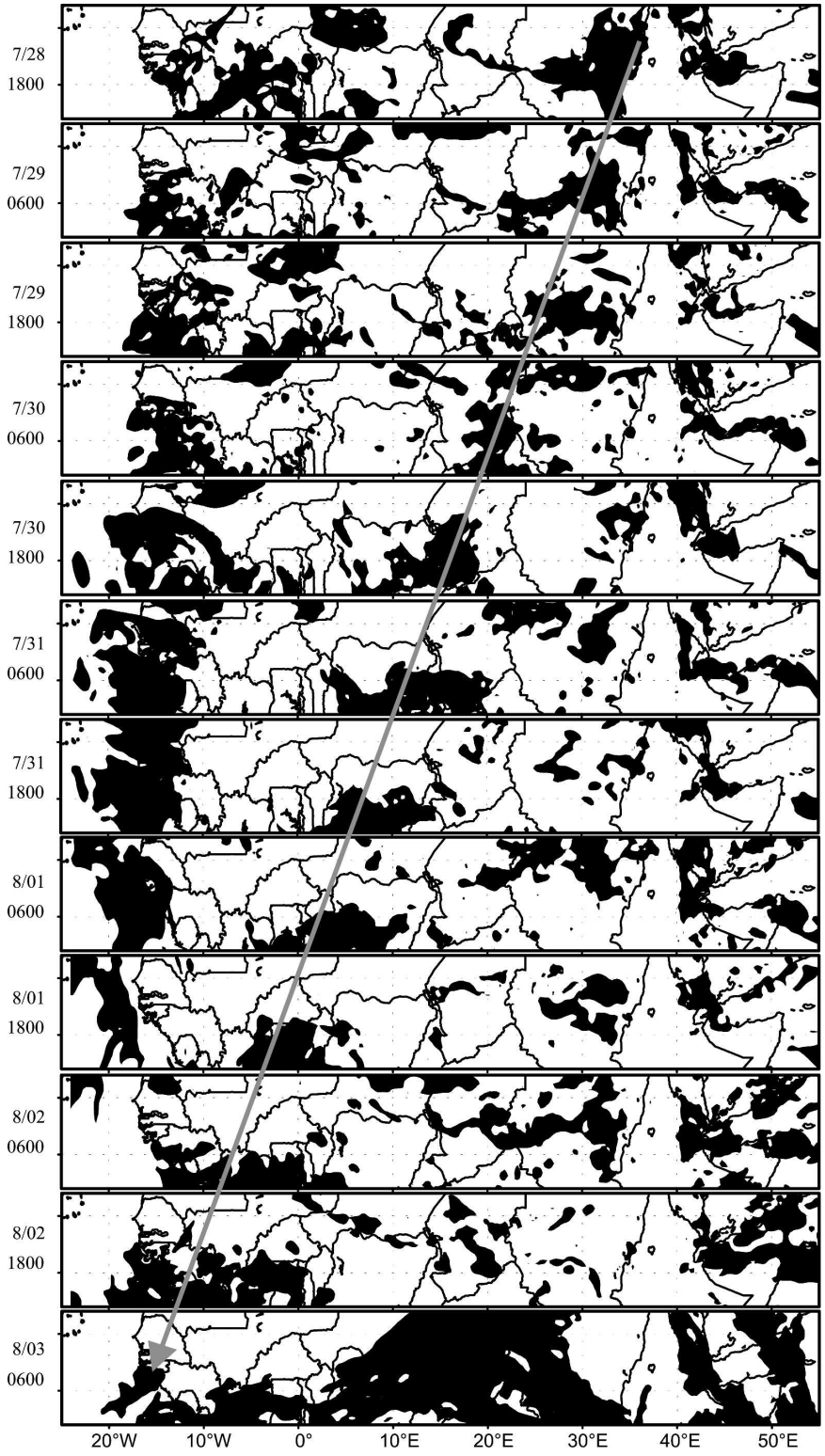

FIG. 12. Specific humidity at the 700-hPa level, from the RegCM3 30-km control case simulation, with values ≥ 7 g kg^{-1} shaded.

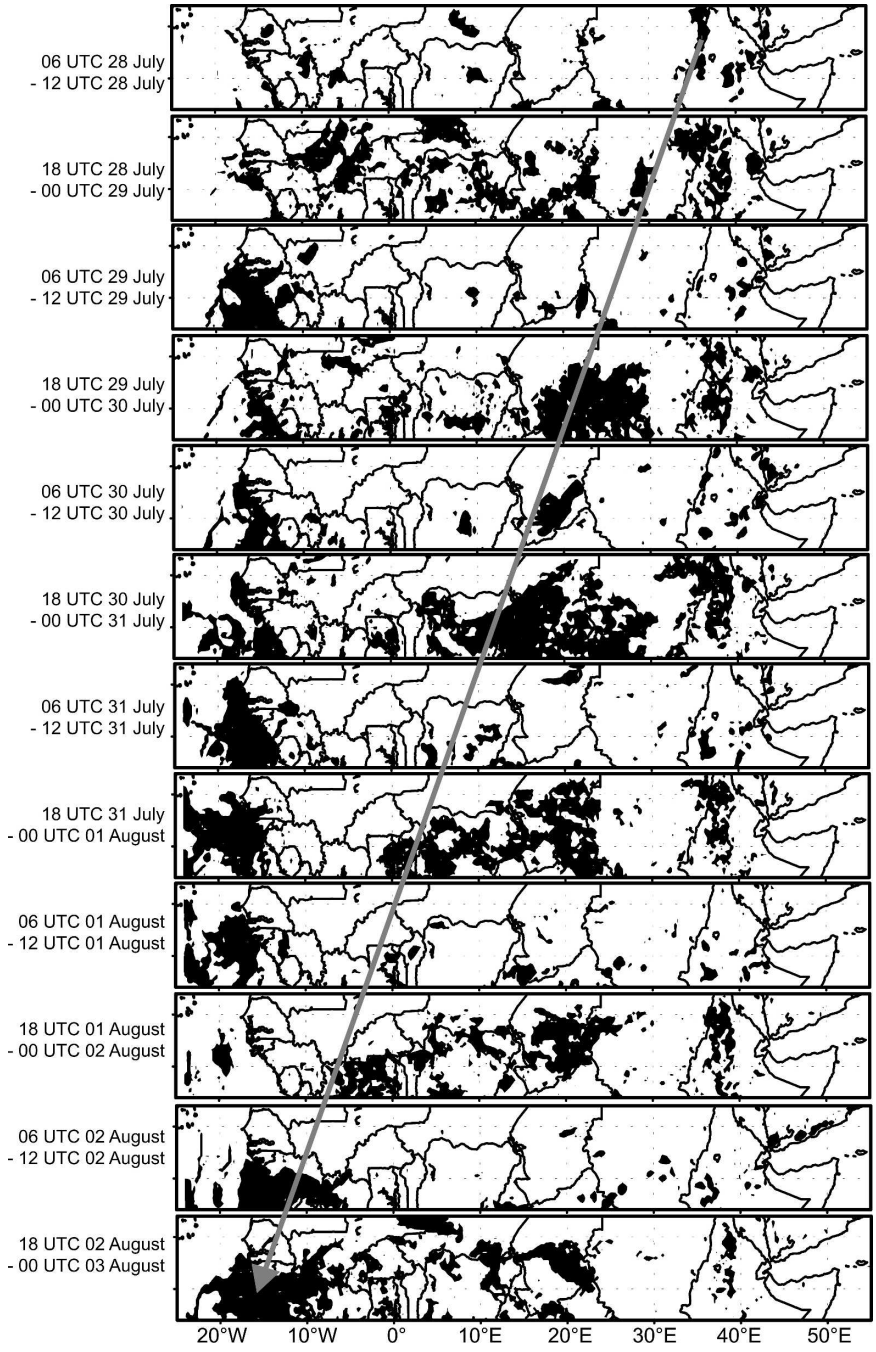

FIG. 13. RegCM3 30-km control case simulation analysis of the total rainfall accumulation for the corresponding 6-h period. Values greater than 10 mm are shaded.

from the RegCM3 30-km real case relative vorticity output (Fig. 10). Using the relative vorticity maxima, the pre-Alberto system embedded in and associated with the AEW feature is observed to have a wavelength of approximately 2700 km, a phase speed of approximately 11.5 m s^{-1}, and a wave period of 2–3 days. This is consistent with the analysis of the EOM data, as presented in section 2, in which the pre-Alberto associative AEW had a wavelength of 2200 km, a phase speed of 11.6 m s^{-1}, and a wave period of 2–3 days.

The pre-Alberto system can also be traced in the 700-hPa potential vorticity (PV) field from the RegCM3 real case simulation, shown in Fig. 11. Throughout its entire convective life cycle the pre-

Alberto system is associated with a strong PV signal with the exception of two times. On 1800 UTC 29 July, when the system is located over western Sudan, the PV signal is less organized and relatively weaker. This time corresponds to the L-I convectively inactive period. The second time in which the PV signature is less organized is 0600 UTC 1 August, when the pre-Alberto disturbance is transitioning from the L-II stage to the G-III stage (Fig. 11). As was seen with the relative vorticity field (Fig. 10), the propagating wave mode and the stationary wave mode can be seen in the PV field.

From a moisture perspective, the RegCM3 30-km real case simulation shows an apparent signal of the pre-Alberto system in both the 700-hPa specific humidity field and the 6-hourly accumulated rainfall (Figs. 12 and 13, respectively). In Fig. 12, the specific humidity associated with the pre-Alberto system is present through its entire life cycle, with only small variations in the overall size of the feature. Rainfall is simulated with the pre-Alberto system in all plots with the exception of two time periods (Fig. 13). Little rainfall is simulated with the pre-Alberto system during the period of 1800 UTC 28 July through 0000 UTC 29 July, in contrast to the observed development of an MCC from satellite data. The second period that is void of significant rainfall is the period of 1800 UTC 31 July to 0000 UTC 1 August, which corresponds to the L-II period (Fig. 13). As seen in the relative and potential vorticity fields at 700 hPa (Figs. 10 and 11, respectively), the propagating and stationary wave modes are apparent in both the specific humidity and in the 6-hourly rainfall accumulations (Figs. 12 and 13, respectively).

From a period starting at about 0600 UTC 31 July to 0600 UTC 2 August, the moisture surrounding the system is relatively confined farther to the south (Fig. 12). Based on a streamline analysis at the 850-hPa level (Fig. 14), the pre-Alberto system (noted by the arrow) is apparently simulated near the lee of the EH region (Fig. 14a). As it travels westward, the pre-Alberto system is influenced by enhanced north-northeasterly flow from the extreme northern portions of central Africa during this particular period. At 0600 UTC 31 July, the approximate center of the pre-Alberto system is located over the southern portion of Chad, as noted in the model output by strong cyclonic turning of the streamlines in this region (Fig. 14b). From this time until roughly 1200 UTC 1 August, the system stays within the influence of the dry northeasterly flow, restricting the availability of moisture, and hence the simulation of rainfall, to the southern portion of the pre-Alberto circulation center (not shown). At approximately 1800 UTC 1 August, the pre-Alberto system is influenced more by a southerly flow regime, allowing moisture

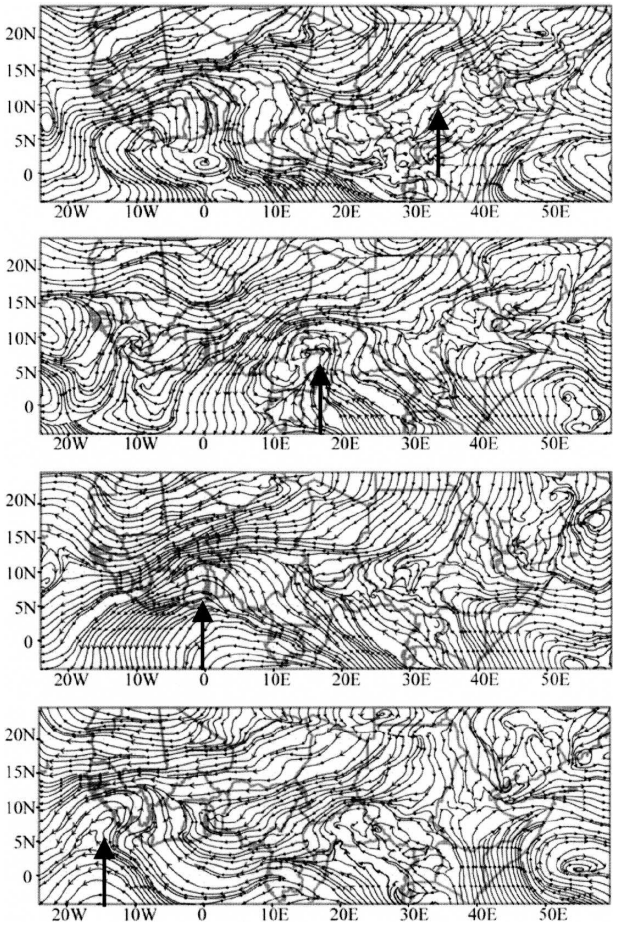

FIG. 14. Streamline analysis at 850 hPa, from the RegCM3 30-km control case simulation, at (a) 1800 UTC 28 Jul, (b) 0600 UTC 31 Jul, (c) 1800 UTC 1 Aug, and (d) 0600 UTC 3 Aug 2000.

from the Gulf of Guinea to entrain into the pre-Alberto system (Fig. 14c). The pre-Alberto disturbance remains in this moist flow regime through the duration of its transcontinental track (Fig. 14d).

Low-level convergence and divergence patterns are good indicators of convective systems. Figure 15 shows the convergence (black) and divergence (gray) at the 850-hPa level from the RegCM3 simulation. A relatively isolated region of convergence can be seen in association with the pre-Alberto system during the entire life cycle of the system. At 0600 UTC 29 July, the convergence region related to the pre-Alberto disturbance is ill defined. This corresponds to the latter part of the G-I stage, when the convection is dissipating and the system is entering the L-I period. At 0600 UTC 1 August and 0600 UTC 2 August the convergence region again becomes relatively weak and disorganized. These two times correspond, respectively, to the very beginning and the end of the G-III period (Fig. 15).

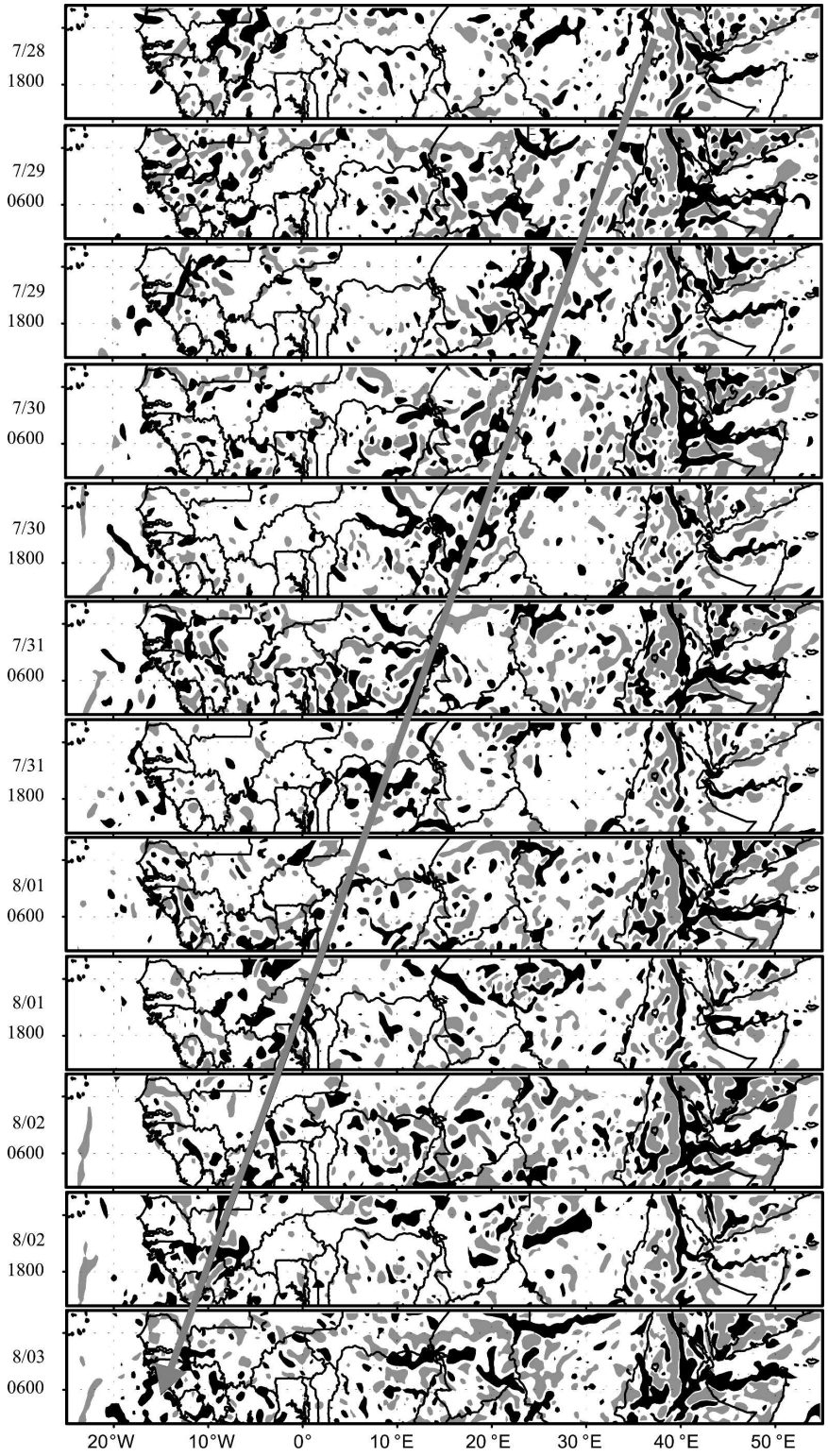

FIG. 15. Convergence (black) and divergence (gray) at the 850-hPa level, from the RegCM3 30-km control case model simulation. Convergence with values $\leq -3 \times 10^{-5}$ s^{-1} is shaded in gray and divergence with values $\geq 3 \times 10^{-5}$ s^{-1} is shaded in black. Black arrow indicates the approximate location of the pre-Alberto system as indicated by the EUMETSAT IR satellite imagery.

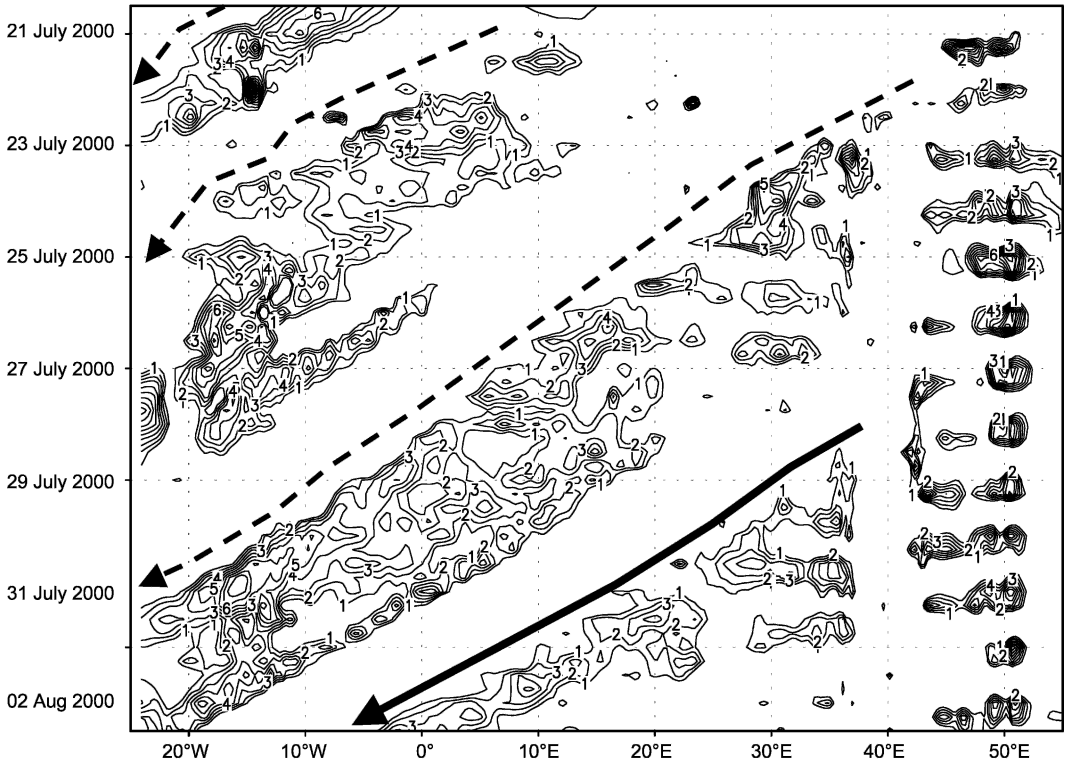

FIG. 16. Meridional wind Hovmöller plot at 700 hPa from the RegCM3 30-km control case simulation. Positive, or southerly, values are contoured at an interval of 1 m s^{-1}. The solid black arrow corresponds to the pre-Alberto system while the dashed lines correspond to wave-type structures associated with other AEWs.

The time–space, or Hovmöller, plot is a good tool for analyzing atmospheric wave disturbances for a composite of a selected variable over a span of time and span of one direction in space. A Hovmöller plot of the 700-hPa meridional winds along the latitude of 10°N is shown in Fig. 16, with southerly wind values contoured at an interval of 1 m s^{-1}. The pre-Alberto disturbance is represented by the west edge of a southerly wind anomaly noted by the solid black arrow in Fig. 16, which is indicative of the westward progression of the system across northern Africa. Throughout the entire pre-Alberto convective life cycle, the system is represented by the west edge of this southerly wind anomaly, originating near the lee side of the EH (~37°E westward) at about 1800 UTC 27 July, approximately 16 h before the onset of the pre-Alberto disturbance (Fig. 16). It continues to move westward and eventually exits from West Africa to over the Atlantic Ocean. The stationary wave mode produced by the EH and the westward-propagating wave mode is simulated to the west and to the east of the EH. Three other westward propagating, AEW-type signatures are also depicted ahead of the pre-Alberto disturbance, as noted by the dashed lines in Fig. 16. The first AEW-type disturbance occurs in the Hovmöller plot from 1200 UTC 20 July near 10°W and moves westward over the Atlantic Ocean on about 0000 UTC 22 July. The second AEW-type signature is first seen around 10°E on approximately 0000 UTC 21 July. The leading edge of this southerly wind anomaly propagates westward and enters the eastern Atlantic Ocean on about 0000 UTC 25 July. A third, prominent anomaly can be followed from the vicinity of the EH on about 0000 UTC 23 July to the west coast of Africa on about 0000 UTC 31 July. These other wave-like disturbances are consistent, in time and space, with satellite observations of cloud clusters over northern Africa (Fig. 2).

A vertical cross section of meridional wind at 10°N from the RegCM3 simulation is shown in Fig. 17. The times shown are at 1800 UTC for (a) 28 July, (b) 31 July, and (c) 1 August 2000, corresponding with the G-I, L-II, and G-III periods, respectively. At any given time in this series, two or three wave-type disturbances can be identified. The pre-Alberto disturbance is first represented by the leading edge of a southerly wind anomaly at about 30°E, extending from the surface to about 750 hPa (Fig. 17a). The anomaly is vertically tilted toward the east from the 750 hPa upward to about

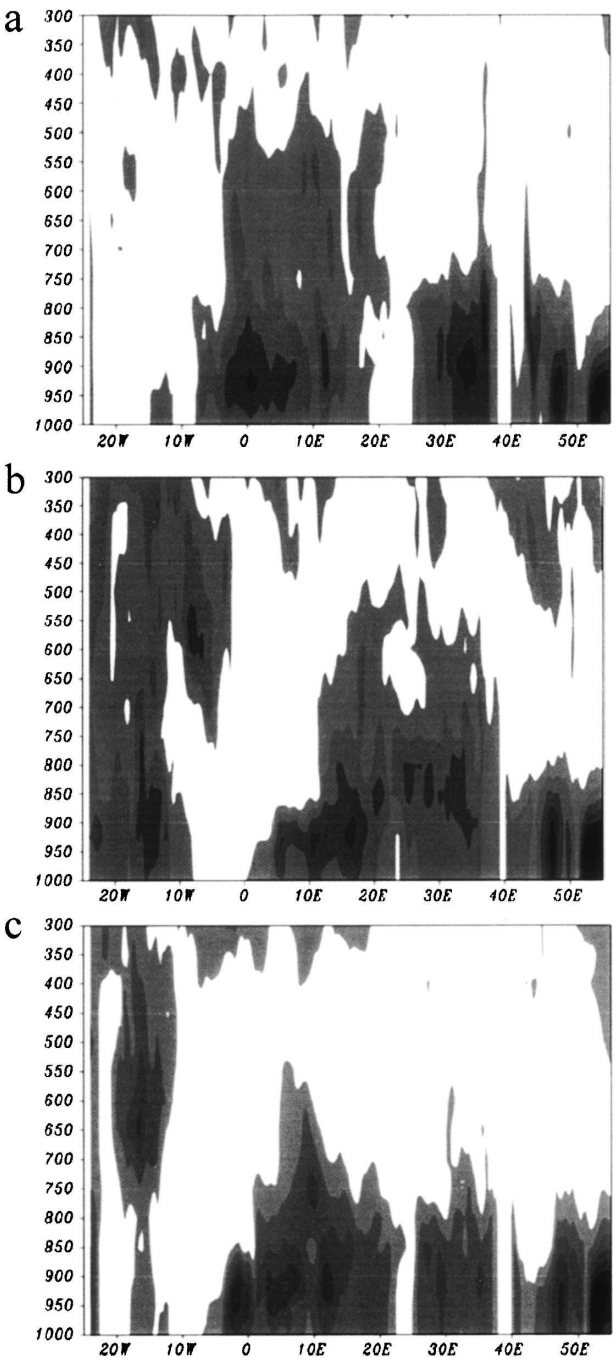

FIG. 17. Vertical cross section of meridional wind (v) fields, from the RegCM3 30-km control case simulation, at 10°N for 1800 UTC on (a) 28 Jul, (b) 31 Jul, and (c) 1 Aug 2000. Areas of $v \geq 1\ \mathrm{m\ s^{-1}}$ are shaded.

300 hPa. Concurrently, a separate southerly wind anomaly is located to the immediate west of the prime meridian and extends upward to about 400 hPa. As this AEW feature moves to the west, the pre-Alberto disturbance continues to organize, as depicted by the increased area and strength of the southerly wind anomaly located near 2°E (Fig. 17b). Here, the anomaly is still slightly tilted vertically to the east starting at 900 hPa. By 1800 UTC 31 July, the southerly wind anomaly, located at about 8°W, is more organized and retains only a slight eastward vertical tilt upward to about 550 hPa (Fig. 17c).

5. Conclusions

Based on the analysis of Meteosat imagery, we found that 23 of 34 tropical cyclones formed over the eastern Atlantic Ocean began as an MCC in the vicinity of the Ethiopian highlands (EH) during the period of 1990 to 2001. We analyzed the *Meteosat-7* IR imagery and EOM analysis data from convective development of the pre-Alberto MCCs from over the EH to the tropical cyclogenesis stage of Alberto over the eastern Atlantic Ocean. We investigated the characteristics of an associated African easterly wave (AEW) and determined the origin point of the AEW to be at the EH.

Seven stages of the convective cycle for the pre-Alberto MCCs were identified: G-I: 1000 UTC 28 July–0830 UTC 29 July; L-I: 0830 UTC 29 July–0200 UTC 30 July; G-II: 0200 UTC 30 July–1400 UTC 31 July; L-II: 1400 UTC 31 July–0200 UTC 1 August; G-III: 0200 UTC 1 August–0000 UTC 3 August; L-III: 0000 UTC 3 August–1200 UTC 3 August; and G-IV: 1200 UTC 3 August–tropical cyclogenesis. The locations where convective genesis and lysis are observed with the pre-Alberto MCCs generally agree with statistical study of HT97, particularly east of 15°E. As was first alluded to by Hill and Lin (2003), the genesis and lysis of the individual African MCCs are linked with a tropical disturbance that would become Hurricane Alberto (2000). In this study, we showed that the pre-Alberto MCCs and MV were embedded within a wavelike disturbance over northern Africa, which is classified as an AEW.

Based on EOM and NCEP moisture datasets, we found that the availability of water vapor is the most essential factor controlling the convective cycle of the pre-Alberto disturbance over the African continent. The presence of significant topography contributes to the generation or decay of the associated MCCs through regulation of the water vapor supply. Four regions of $\overline{\mathrm{RH}} \geq 90\%$ along about 10°N were collocated with significant topography. Adiabatically warmed downslope flow from the Ruwenzori Mountains and Cameroon highlands, along with the entrainment of dry air from the Sahara Desert, likely suppressed moist convection associated with the pre-Alberto disturbance. Based on the present study, orographic forcing led to the development of a pre-Alberto MCC at the

EH during the G-I stage and at the Darfur Mountains and the Bongo Massif during the G-II stage. The presence of orography, therefore, affects the cycle of convective development within an AEW. This concept will be further investigated in a future study.

The pre-Alberto MCC was one of several MCSs observed over the African continent and embedded in an AEW during the period of interest; one can identify three MCSs existing concurrently over the African continent. At the EH, there existed two modes of disturbance development: a stationary mode and a propagating mode. The stationary mode corresponded with the generation of moist convection over the EH. The propagating mode corresponded with the generation, and the westward propagation, of MVs and MCSs from the lee side of the EH.

To prove that disturbances generated at the EH are indeed AEWs, we used the NCAR Regional Climate Model Version 3.0 (RegCM3) to simulate the event. The propagating wave mode, associated with the westward progression of the AEW, and the stationary mountain-induced wave mode, located at about 40°E near the EH region, are both present in the fields of relative vorticity, potential vorticity, specific humidity, and 6-hourly rainfall. In general, the simulated fields showed that the convection was indeed generated over the EH and the pre-Alberto disturbance was generated at the lee of the EH. In addition, the convective cycle detected in the EOM data was also reflected in the simulated fields. Simulated AEW characteristics can also be deduced from the RegCM3 30-km real case results. Using these fields, the pre-Alberto system embedded in and associated with the AEW-like feature is observed to have a wavelength of approximately 2700 km, a phase speed of approximately 11.5 m s^{-1}, and a wave period of 2–3 days. This is consistent with EOM analyses, in which the pre-Alberto AEW had a wavelength of 2200 km, a phase speed of 11.6 m s^{-1}, and a wave period of 2–3 days. In summary, analysis of the model results indicate that the convection associated with the incipient MCC, and the pre-Alberto AEW itself, originated near the EH.

Acknowledgments. The authors thank Dr. Simon Chang for his helpful insight and discussions that assisted in the production of this paper. The authors would also like to thank Dr. Fredrick Semazzi and Richard Anyah for their assistance with the Regional Climate Model. Satellite data were obtained from the Meteorological Archiving and Retrieval Facility of the European Organisation for the Exploitation of Meteorological Satellites (EUMETSAT) based in Darmstadt, Germany. The EOM datasets were obtained directly from the Meteorological Applications Section of the Operations Department of the European Centre for Medium-Range Weather Forecasts (ECMWF) based in Reading, United Kingdom. NCEP reanalysis data were obtained from the Climate Diagnostics Center of NOAA. The research presented herein is supported by the Office of Naval Research under Grant N00014-02-1-0674.

REFERENCES

Berry, G. J., and C. Thorncroft, 2005: Case study of an intense African easterly wave. *Mon. Wea. Rev.,* **133,** 752–766.

Bister, M., and K. A. Emanuel, 1997: The genesis of Hurricane Guillermo: TEXMEX analyses and a modeling study. *Mon. Wea. Rev.,* **125,** 2662–2682.

Carlson, T. N., 1969: Synoptic histories of three African disturbances that developed into Atlantic hurricanes. *Mon. Wea. Rev.,* **97,** 256–276.

Chang, C. P., 1970: Westward propagating cloud patterns in the tropical Pacific as seen from time-composite satellite photographs. *J. Atmos. Sci.,* **27,** 133–138.

——, V. F. Morris, and J. M. Wallace, 1970: A statistical study of easterly waves in the western Pacific: July–December 1964. *J. Atmos. Sci.,* **27,** 195–201.

Dickinson, R., A. Henderson-Sellers, and P. Kennedy, 1993: Biosphere–Atmosphere Transfer Scheme (BATS) version 1e as coupled to the NCAR Community Climate Model. NCAR Tech. Note NCAR/TN-387+STR, 80 pp.

Farfán, L. M., and J. A. Zehnder, 1997: Orographic influence in the synoptic-scale circulations associated with the genesis of Hurricane Guillermo. *Mon. Wea. Rev.,* **125,** 2683–2698.

Fritsch, J. M., and C. F. Chappell, 1980: Numerical prediction of convective driven mesoscale pressure systems. Part I: Convective parameterization. *J. Atmos. Sci.,* **37,** 1722–1733.

Gray, W. M., 1968: Global view of the origin of tropical disturbances and storms. *Mon. Wea. Rev.,* **96,** 669–700.

——, 1998: The formation of tropical cyclones. *Meteor. Atmos. Phys.,* **67,** 37–69.

Grell, G. A., 1993: Prognostic evaluation of assumptions used by cumulus parameterizations. *Mon. Wea. Rev.,* **121,** 764–787.

Hill, C. M., and Y.-L. Lin, 2003: Initiation of a mesoscale convective complex over the Ethiopian Highlands preceding the genesis of Hurricane Alberto (2000). *Geophys. Res. Lett.,* **30,** 1232, doi:10.1029/2002GL016655.

Hodges, K. I., and C. D. Thorncroft, 1997: Distribution and statistics of African mesoscale convective weather systems based on the ISCCP Meteosat imagery. *Mon. Wea. Rev.,* **125,** 2821–2837.

Holton, J. R., 1970: A note on forced equatorial waves. *Mon. Wea. Rev.,* **98,** 614–615.

——, 1971: A diagnostic model for equatorial wave disturbances: The role of vertical shear of the mean zonal wind. *J. Atmos. Sci.,* **28,** 55–64.

Holtslag, A. A. M., E. I. F. de Bruijn, and H.-L. Pan, 1990: A high resolution air mass transformation model for short-range weather forecasting. *Mon. Wea. Rev.,* **118,** 1561–1575.

Laing, A. G., and J. M. Fritsch, 1993: Mesoscale convective complexes in Africa. *Mon. Wea. Rev.,* **121,** 2254–2263.

Maddox, R. A., 1980: Mesoscale convective complexes. *Bull. Amer. Meteor. Soc.,* **61,** 1374–1387.

Mozer, J. B., and J. A. Zehnder, 1996: Lee vorticity production by large-scale tropical mountain ranges. Part II: A mechanism

for the production of African easterly waves. *J. Atmos. Sci.,* **53,** 539–549.

Nitta, T., 1970: Statistical study of tropospheric wave disturbances in the tropical Pacific region. *J. Meteor. Soc. Japan,* **48,** 47–60.

Pal, J. S., E. E. Small, and E. A. B. Eltahir, 2000: Simulation of regional-scale water and energy budgets: Representation of subgrid cloud and precipitation processes within RegCM. *J. Geophys. Res.,* **105,** 29 579–29 594.

Piersig, W., 1936: Variations of pressure and winds, a treatise on the weather of trade wind region of eastern North Atlantic (in German). *Archiv Deut. Seewarte,* **54** (6). (English translation of Parts 2 and 3, *Bull. Amer. Meteor. Soc.*, **25**, 2–16).

Reed, R. J., D. C. Norquist, and E. E. Recker, 1977: The structure and properties of African wave disturbances as observed during phase III of GATE. *Mon. Wea. Rev.,* **105,** 317–333.

Regula, H., 1936: Druckschwankungen und Tornados an der Westkuste von Afrika. *Ann. Hydrogr. Mar. Meteor.,* **64,** 107–111.

Riehl, H., 1945: Waves in the easterlies and the polar front in the tropics. Miscellaneous Rep. 17, Dept. of Meteorology, University of Chicago, 79 pp.

——, 1948: On the formation of typhoons. *J. Meteor.,* **5,** 247–264.

Simpson, J., E. Ritchie, G. J. Holland, J. Halverson, and S. Stewart, 1997: Mesoscale interactions in tropical cyclone genesis. *Mon. Wea. Rev.,* **125,** 2643–2661.

Simpson, R. H., N. L. Frank, D. Shideler, and H. M. Johnson, 1968: Atlantic tropical disturbances 1967. *Mon. Wea. Rev.,* **96,** 251–259.

Thorncroft, C. D., and B. J. Hoskins, 1995: An idealized study of African easterly waves. I: More realistic basic states. *Quart. J. Roy. Meteor. Soc.,* **121,** 1589–1614.

Wallace, J. M., and C. P. Chang, 1969: Spectra analysis of large-scale wave disturbances in the tropical lower troposphere. *J. Atmos. Sci.,* **26,** 1010–1025.

Yanai, M., T. Maruyama, T. Nitta, and Y. Hayashi, 1968: Power spectra of large scale disturbances over the tropical Pacific. *J. Meteor. Soc. Japan,* **46,** 308–323.

Zeng, X., M. Zhao, and R. E. Dickinson, 1998: Intercomparison of bulk aerodynamic algorithms for the computation of sea surface fluxes using TOGA COARE and TAO data. *J. Climate,* **11,** 2628–2644.